Memoirs of the Faculty of Engineering, Nagoya University
Vol. 39, No, 2 (1987)

DYNAMICAL STUDIES OF MICROSTRUCTURAL CHANGES OF CRYSTALS BY REAL TIME X-RAY TOPOGRAPHY

TORU IMURA, HIROYASU SAKA, TATSUMASA KOBAYASHI, NOZOMU KAWABE, AKIRA SAKAI and HISAAKI SUGA

Department of Metallurgy

(Received October 31, 1987)

Abstract

Crystal growth of pure aluminum, pure gallium and aluminum-magnesium alloys has been studied by real time x-ray topography using an ultra high intensity x-ray generator and a Lang-type camera with a heating facility.

Faceted growth has been observed in gallium, but not in aluminum. In both cases, however, a dislocation free region has been observed near the solid-liquid interface. Many dislocations were generated behind this region as the interface advanced and also as the growth rate was suddenly changed. Based on the present observations, it is concluded that the Jackson's theory has to be modified at least by taking into account the contribution of the second nearest neighbor atoms in calculating α-parameter. In the case of aluminum-magnesium alloys, it is found that the angle between the primary arm and the secondary arm of a dendrite changes depending on growth rate and solute content.

Origin of dislocations induced during crystallization and cooling process are critically discussed and the most probable origin is considered to be vacancy condensation.

Effectiveness of thermal cyclic annealing in the reduction of dislocation density in various types of crystal is experimentally confirmed.

CONTENTS

1. Introduction

Crystal growth from the melt has been most widely used to prepare large single crystals of metals, alloys and semiconductors. Many theoretical as well as experimental investigations have been made to understand the mechanism of crystal growth from the melt. However, our understanding of the mechanism of crystal growth is still insufficient, particularly, in the case of opaque substance like metals. The reason for this is mainly due to the fact that detailed experimental studies of the kinetics of the melt growth and the mechanism of growth are difficult and therefore scare. Direct observations of the interfacial morphology of growing crystals are considered to be an effective way of investigating the growth mechanism. The observation of the behavior of crystal defects during growth can also give particularly useful information on the mechanism of growth from the melt. For example, the effect of screw dislocations on faceted growth, observed in Si,[1)~4)] is an evidence for the fact that the surface of a crystal in contact with its melt is not rough but smooth on the atomic scale, and that the nucleation for growth occurs at the intersections of dislocations.

Real-time observation has been performed by several investigators to study the kinetics of the crystal growth from the melt by optical microscopy, [5)~13)] electron microscopy[14)~16)] and x-ray topography.[17)~19)] However, since it is almost impossible to observe the solid-liquid interface of opaque substances such as metals directly by optical microscopy, there is only one direct observation of interface morphology and the behavior of crystal defects during growth by this method.[20)] Transmission electron microscopy can provide very high resolution[21)~23)] and enables defect structure during the growth to be observed, but the growth rate to be studied is severely limitid by the large magnification, and the extreme thinness of the specimens used may result in the observation of a growth process different from ordinary macroscopic scale growth.[24)] X-ray topography, on the other hand, allows us to investigate not only macroscopic growth but also dislocation behavior during growth even while varying growth factors such as the growth rate, temperature gradient, atmosphere, etc. For this reason, in spite of its low magnification, x-ray topography has been used in investigating crystal growth from the melt. Kobayashi et al.[17,18)] and Nittono et al.[19)] observed the behavior of dislocations during the growth of large Al and Sn crystals dynamically by x-ray topography, respectively.

To investigate the effect of dislocations on faceted growth, growth conditions which control the presence or absence of dislocations must be used. Gallium is a suitable material for such control and for the study of growth kinetics, since it is readily available at very high purity, and when it is very pure, dislocation-free crystals can be grown with relative ease. Jackson's α-parameter[25)] for gallium is greater than 2 on the (010) face and nearly 1 on other faces. According to Jackson's theory,[26,27)] some habit planes (facets) are expected to appear in gallium crystals during the growth from the melt, although in the case of Al, α is less than 2 for all orientations so that the facets are not expected to appear.

The primary aim of the present studies is to clarify the growth machanism and the origins of dislocations by carrying out an observation of the interface morphology and the effect of dislocations on it during the growth from the melt using real-time x-ray topography.

Besides this, observations on the sequential growth and morphology of dendrite arms during solidification, and the reduction of density of dislocations due to thermal cyclic annealing of Ag and Ag alloys, Fe-3 % Si alloys and Si, have been made by real-time x-ray topography to obtain valuable information which can not be obtained by conventional "ex post fact" method.

2. Real-Time X-Ray Topographic Study of Crystal Growth from the Melt

2. 1. Real-Time X-Ray Topography Apparatus

For real-time observation of melting and growth processes of metallic crystals, an x-ray diffraction topographic system which consists of a 90 kW-class high power x-ray generator (RU-1500, Rigaku Denki), a large topographic goniometer of Lang type and a TV-VTR imaging system was employed.[28~30] In the present experiments, the x-ray generator with Ag target was operated at 50kV, 1200 mA (with a bias voltage of 1000 V) and Ag K_α radiation was used for topography. For reflection topography, Cu K_α radiation from a rotating Cu target was used under the operating condition of 55 kV, 1300 mA. The effective size of the focus was 1.0×1.0 mm and the distance between the focus and the specimen was 1200 mm, so that the geometrical resolution was about 3μm in the horizontal direction and 25 μm in the vertical direction. A block diagram of the topographic system used is shown in Fig. 1.

The goniometer used was of a Lang camera type, which can be used for both Lang method and Berg-Barrett method in the present case. The distance between the x-ray source and the specimen was 1200 mm and that between the specimen and the film or the TV camera was 6 and 80 mm, respectively. The remote control of θ adjustment, sample rotation and selection of the imaging area can be made. The geometry of the imaging system is schematically shown in Fig. 2.

The TV imaging system consists of a TV camera unit with a PbO vidicon tube (Hamamatsu Photonics, N-603, imaging area: 12×9 mm, spacial resolution: 20-25 μm), a video amplifier, a camera control unit, a digital image processor (Aviotronics, Image Σ) and a TV monitor operating as a normal closed-circuit TV system (cf. Fig. 2). The TV frame speed is 30 frames/s and the number of scanning lines is 525. By orienting the crystal so as to satisfy the Bragg condition for a slightly divergent incident beam, two images due to the diffracted $K\alpha_1$ and $K\alpha_2$, each of which has a width of 1 mm, are received by the vidicon tube, where two band-shaped images are directly converted into video signals and displayed simultaneously on the TV monitor screen with a magnification of about 20 times. Such images are referred to as "direct view images".[31] To observe a larger area of the specimen, the video signals due to $K\alpha_1$ (or $K\alpha_2$) are selected electrically and stored in the image storage, while the goniometer is oscillated between $\pm40'$ (θ oscillation topography). The electric slit is also oscillated in synchronization with the selected $K\alpha_1$ (or $K\alpha_2$) image, and at the end of the oscillation, a Lang

topograph with the imaging area of the vidicon tube ($9\times12\,mm^2$) is displayed on the TV monitor. Such images are referred to as "synthesized images"[31] hereafter. The dynamic behaviors of the solid-liquid interface and dislocations near the interface during melting and growth processes were recorded by a video tape recorder (VTR) in parallel with the observation. However, if the signal-to-noise ratio (S/N ratio) of an image was not high enough to observe images of individual dislocations, the S/N ratio was improved, if necessary, by averaging of n frames of TV images with the digital image processor. The averaging of n TV frames improves the S/N ratio by a factor of $(2n-1)^{1/2}$. This image processing was made for both "direct-view image" and "synthesized image". As the spacial resolution of the TV imaging system was lower than the geometrical one, the images were also recorded intermittently on Ilford-L4 nuclear research plates to reveal the details of dislocation configuration or to determine the Burgers vector of dislocations by the invisibility criterion.

2. 2. Heating Device for Observations of Unidirectional Growth

For the observation of unidirectional melting and growth processes of metallic crystals by real time x-ray topography, two types of in-situ heating furnaces were developed, both of which can be set on the topographic goniometer stage.[17,32]

Fig. 3 (a) and (b) show the whole view and schematic illustration of the furnace with a graphite heater. The furnace is composed of a vacuum chamber with Be windows, a graphite heater which can be moved up and down, and a graphite crucible with hot junctions of thermocouples. Any temperature up to about 1200 K can be obtained. The water-cooled furnace is either evacuated to 1×10^{-4} Torr or filled with a desired environmental gas. The depth of the vacuum chamber, i. e., the distance between the specimen and the Be window located on the side of the TV camera was made narrow enough to get better resolution. The graphite heater can be moved up and down by rotating a micrometer screw, which is driven by a synchronous motor through a worm gear. This enables us to grow crystals in a constant temperature gradient near the solid-liquid interface. A plate-shaped specimen of a single crystal is put in the graphite crucible and heated by the graphite heater from both sides of the crucible. Graphite is very suitable for the crucible of this furnace because it is sufficiently unreactive chemically to aluminum and its alloys below 1070 K and x-ray beams are little absorbed by it. The crucible consists of three graphite plates, and the two plates which contact with front and back surfaces of the specimen are about 0.5 mm in thickness. The outside size of the crucible is about 50 mm(long) $\times$ 10 mm(wide) $\times$ 2 mm(thick). The temperature of the specimen is measured by chromel-alumel thermocouple of 0.1 mm in diameter, the surface of which is coated with ceramics and which is contacted with the specimen. The temperature gradient of the specimen obtained is about 10K/mm. (cf. Fig. 4).

The furnace has two Be windows of 46 mm in diameter on either side of it. Incident and diffracted x-ray beams pass through the Be windows, the graphite heater and the graphite crucible. To examine the influence of these graphite plates on the spatial resolution, topographs of a silicon crystal interposed between graphite plates (1 mm in thickness) and the crystal without graphite plates were taken by the Lang method, which are shown in Fig. 5. As is seen in Fig. 5, it can be concluded that graphite plates have little influence on the resolution of topographic images.

Fig. 6 shows a schematic illustration of another type of the furnace for unidirectional solidification. In this case, the crucible which contains a specimen is heated by four metallic resistors. These heaters consist of alumina cores and Ni-Cr wires of 0.6 mm in diameter which are wound around the cores. By adjusting the current of the upper and the lower heaters, the temperature gradient of the specimen can be changed in the range of 0.7 K/mm to 1.2 K/mm. The typical temperature gradient of the specimen near the melting point (873 K-933 K) was 1.0 K/mm, as shown in Fig. 7. Solidification was brought about by decreasing the temperature of the heaters slightly. In this case, there is a possibility of variation of the temperature gradient on the specimen near the solid-liquid interface, but it had little influence on the morphology of the interface or behavior of crystal defects (the variation of the temperature gradient near the interface can roughly be estimated less than 10^{-1}K/mm), as shown in the later chapter. The crucible used for this furnace was almost the same as that for the furnace with a graphite heater (cf. Fig. 4.). Other conditions of the observation were the same as in the case of the aforementioned furnace.

In the observation of melting and growth processes of gallium single crystals, a graphite crucible of modified type was used which is shown in Figure 8 with the geometry of the imaging system. A plate-shaped specimen of gallium single crystal specimen was put in the graphite crucible, inside of which was covered by Teflon sheets. The crucible and the specimen were heated by the upper resistance heater of the furnace shown in Fig. 6, resulting in unidirectional melting and growth. The temperature gradient of the specimen was about 0.4 K/mm.

With these apparatuses, real time observations of melting and growth processes of single crystals of aluminum, gallium and Al-Mg binary alloys have been made. The specimen was melted from the upper part to the lower part unidirectionally in pure argon gas atmosphere. Melting was interrupted from time to time, leaving part of the specimen unmolten (cf. Fig. 9). After keeping it in equilibrium for a while, the growth was started from the seed (the unmolten part) unidirectionally upwards.

2. 3. Growth of Single Crystals of Pure Aluminum

2. 3. 1. Experimental Procedures

Specimens used in this study were single crystals of two grades of purity, the compositions being shown in Table 1. These single crystals were grown either by strain-anneal method or the Bridgman method. The final dimension of the specimens used was 30 mm×4 mm×(0.7−0.8) mm.

Table 1. Composition of aluminum single crystals

	Cu%	Fe%	Si%	Zn
99.998% Al	0.0004	0.0009	0.0003	tr.
99.999% Al	0.00008	0.0010	0.0000..	tr.

The measurement of supercooling was made using chromel-alumel thermocouples of 0.1 mm in diameter, the surface of which was ceramic-coated and which was placed in contact with the specimen. Two types of crucible, indicated schematically in Fig. 10 were used. The crucible shown in Fig. 10 (a) was used for measuring supercooling. In this crucible, two sets of thermocouples were connected in such a way as indicated in Fig. 10 (a) in order to measure the difference between the

temperature of the crystal and that of the melt near the interface. The distance between the two junctions of the thermocouples was about 1mm. The electromotive force was amplified and then recorded on a recorder. Fig. 10 (b) shows the crucible used for the measurement of cooling rate. A slight change of the temperature in the specimen can be detected. The growth rate was measured from the photographs of the images on the TV monitor. Measurements for the kinetic study were made on crystal growth in ⟨100⟩, ⟨110⟩ and ⟨111⟩ directions.

2. 3. 2. Observations of Solid-Liquid Interface

Melting process of aluminum single crystals

Fig. 11 shows a series of transmission x-ray topographs obtained during a unidirectional melting process of aluminum (99.998 % in purity) using the furnace shown in Fig. 3. All the topographs were reproduced through an image processor from TV images and in negative contrast. Therefore, crystal defects such as dislocations show up as black images. The temperature gradient of the specimen at the temperature near the melting point was about 10 K/mm. Fig. 11. (a) was obtained at room temperature. The broad images observed at the lower part are subgrain boundaries. Fig. 11 (b) shows the state just before the melting began. A number of dislocations were generated by thermal stresses in a temperature range from 670 K to 930 K during heating up to the melting point.

Fig. 11 (c)～(e) illustrate the images taken during the melting process. When the melting began from the upper part of the specimen to the lower part unidirectionally, a macroscopically straight interface was observed along the isothermal plane of the specimen, and no fringe due to thickness variation was observed. This indicates that the temperature gradient in the specimen was nearly completely unidirectional. The surface of the crystal in contact with the melt was indicated by bold arrows. In Fig. 11 (c)～(e), the upper region, which was the molten part, shows no contrast because the Bragg reflection does not take place in the melt. It can be seen that the region of the crystal near the interface shows no anomalous contrast before the melting, and perfection of the region was almost the same as that before the melting. These observations showed that most of the dislocations were immobile until they come into contact with the interface during melting. The mean melting rate was estimated to be about 12 μm/s from the topographs.

Fig. 12 shows similar series of topographs of TV images taken during the melting process of aluminum single crystal (99.998 % in purity) but under the condition of a smaller temperature gradient (1.0 K/mm) using the furnace shown in Fig. 5. The solid-liquid interface, which is indicated by bold arrows, lay along isotherms of the crystal. Black lines caused by bundles of many dislocations are seen in the crystal and they intersect with the interface almost perpendicularly. In accordance to the results shown in Fig. 11, no contrast anomaly was observed along the interface and the dislocation bundles did not move until they came into contact with the interface.

Another observation of the melting process of aluminum (99.998 % in purity) was made where the solid-liquid interface advanced horizontally (the temperature gradient was 1.0 K/mm). Fig. 13 (a) and (b) were taken during the melting process and (c) in the equillibrium state. The broad black lines which contact with the interface obliquely are subgrain boundaries. Again in this case, macroscopical solid-liquid interface was observed to lie along the isothermal plane.

Growth process of aluminum single crystals

Fig. 14 is a series of topographs taken on the same crystal shown in Fig. 11 during a crystal growth. The mean growth rate was about 20 μm/s in Fig. 14 (a) to (c). The solid-liquid interface (indicated by bold arrows) is macroscopically flat and extends along the isotherms of the crystal. The boundary between the seed crystal (unmolten part of the crystal) and the newly grown crystal is indicated by a broken line. Comparison between Fig. 11 with Fig. 14 shows that the perfection of the crystal just after the solidification (in Fig. 14) is better than that of the seed (cf. Fig. 11). Dislocation bundles, which were inherited from the seed (indicated by the arrow with dg,) intersected with the interface and disappeared out of the crystal in the early stage of the growth.

Contrast anomaly, which has been reported to be observed in Si,[3] is not observed in the melt near the solid-liquid interface. In order to confirm that no contrast anomaly is associated with the solid-liquid interface, the solid-liquid interface was observed using the reflection perpendicular to that used in Fig. 15. This was carried out by observing the process of growth in the horizontal direction with a vertical isothermal plane (Fig. 15), continued from the equilibrium state shown in Fig. 12 (c). The growth rate was 19 μm/s. The reflecting plane was nearly parallel to the solid-liquid interface. No contrast anomaly along the interface was observed in this case, either. This "contrast experiment" shows definitely that in the case of high-purity Al (99.998 %) no contrast anomaly is associated with the solid-liquid interface unlike Si.

Fig. 16 shows effects of growth rate on the perfection of Al single crystal (99.999 %). The growth rate between (a) and (c) was about 20 μm/s and that between (d) and (f) was about 45 μm/s. It is obvious that the perfection of a slowly grown crystal is better than that of a rapidly grown one.

A similar observation of other crystals showed that when a crystal is grown at a rate greater than a certain rate (about 40 μm/s in the present case) many dislocations are suddenly generated in the newly grown region of the crystal. No contrast anomaly along the solid-liquid interface was observed in the case of rapid growth, either.

2. 3. 3. Growth Kinetics and Measurement of Growth Rate

The measurement of super-cooling using the crucible shown in Fig. 10 was unsuccessful, because the supercooled layer in the melt is too narrow to be detected by means of thermocouples of 0.1 mm in diameter. Therefore, super-cooling of the melt was determined from cooling curves measured using the crucible shown in Fig. 10 (b).

Fig. 17 shows typical heating and cooling curves measured during melting and growth processes of aluminum crystal (99.999 %) under condition of high temperature gradient (10 K/mm). Each point on the curves indicated by arrows shows the temperature measured at the moment when the solid-liquid interface passed through the hot junctions of the thermocouple.

Fig. 18 shows the relations between growth rate and super-cooling measured from the cooling curves during the growth in the [110] and [111] directions. It is obvious from the graph that growth in the [111] direction is more rapid than that in the [110] direction. This may be surprising, because growth kinetics of aluminum in the [110] and [111] directions has been believed to be that of normal (or adhesive) growth. However, the growth kinetics obtained in this experiment

may not be very accurate, because many dislocations are most likely generated around the thermocouple in contact with the melt.

2. 4. Growth of Single Crystals of Gallium

2. 4. 1. Experimental Procedures

Specimens of gallium single crystals used were prepared from nearly dislocation-free single crystals grown by the Bridgman method. Procedure for preparation of specimens for the x-ray topographic observatins is schematically illustrated in Fig. 19. The starting material was gallium of 99.9999% in purity and its composition is shown in Table 2. Crucible of vinyl resin, which contained gallium of 15mm in diameter, was put into a glass container filled with water which was kept at about 305 K. After the gallium bar had been completely melted, the glass container was gradually cooled down below the melting point of gallium (302.8 K). Because the temperature of the water in the container was lower in the lower part than that in the upper part, a gallium single crystal of 15 mm in diameter and about 40 mm in length was grown upward in such a container. In spite of this simple method, nearly dislocation-free (dislocation-free except for region near the surfaces) single crystals of high-purity gallium were grown with relative ease. These crystals were cut with the aid of a multi-wire saw into slices of about 0.25 mm thick for transmission x-ray topography and 0.85 mm thick for reflection x-ray topography, respectively. Finally, each slice was cut into a size of about $20\times4\,mm^2$, and polished mechanically with an emery paper, followed by electropolishing using the solution of 1 part $HClO_4$ and 4 parts CH_3OH (by volume). The final thickness of the specimens was 0.1 mm for transmission topography and 0.6 mm for reflection topography.

Table 2. Composition of gallium slngle crystals

Mg ppm	Al ppm	Si ppm	Ca ppm
0.03	0.3	0.03	0.04

2. 4. 2. Observation of Solid-Liquid Interface

Melting process of gallium single crystals

Fig. 20 is a series of reflection topographs of TV images taken during the melting process of a gallium single crystal. The direction of temperature gradient was normal to the solid-liquid interface indicated by bold white arrows. Fig. 20 (a) and (b) are images during melting and Fig. 20 (c) is that in the equilibrium state. The temperature gradient in the crystal was about 0.4 K/mm. The broad images observed on the right hand side of the specimen were dislocations introduced during the preparation of the specimen. Neither an equal-thickness fringe nor any intensity anomaly was observed in the vicinity of the interface during the melting or in the equilibrium state. This is in good agreement with the results obtained on aluminum.

Growth process of gallium single crystals

Many types of facet plane which were inclined to the isothermal plane in the liquid were observed during unidirectional solidification of gallium single crystals.

A typical example of TV images of the transmission topography of such faceted growth is shown in Fig. 21. In this case, two crystallographically equivalent {011} facets appeared and competed with each other. Each facet is inclined to the isothermal plane to gain the supercooling required for faceted growth, and the nucleation for growth takes place at the corner of right- and left- sides for the (011) and (0$\bar{1}$1) facet, respectively. In Fig. 19 (a), many black lines due to bundles of dislocations are visible and some of them are left behind the facet although two bundles of dislocations intersect with the right (0$\bar{1}$1) facets. By examining their image contrast with various reflections after growth, it is found that they have no common Burgers vector. However, this facet does not shrink by the intersection of the dislocation bundles. Moreover, these bundles are also left behind and the newly grown region of the crystal seems to be free from dislocations, as seen in Fig. 19 (c) and (d). In this case, the dislocation bundles which intersected with the interface almost perpendicularly did neither propagate into newly grown crystal nor influence the faceted growth.

In another case, dislocation bundles, which propagated into a newly grown crystal and intersected with the interface, were observed, as shown in Fig. 22. Fig. 22 is a series of TV images taken during the growth process by reflection topography. Fig. 22 (a) shows the seed crystal just before the growth started. The macroscopic interface lies along the isothermal plane, and a broad black line which is the image of a bundle of many dislocations is observed. As the crystal grew (cf. Fig. 22 (b)), ($\bar{1}$10) and (010) facets appeared, and the dislocation bundle propagated into the newly grown crystal. If nucleation occurred at the intersection of the bundle, ($\bar{1}$10) facet, which is inclined to the isothermal plane, would not appear. Moreover, ($\bar{1}$11) and (011) facets appeared as in Fig. 22 (c) and the dislocation bundle propagated into newly grown crystal without affecting the faceted growth.

Similar behavior of dislocations was observed in the transmission topographs as shown in Fig. 23. In Fig. 23 (a), which is the TV image of growth process, many dislocations intersect with ($\bar{1}$01) and ($\bar{1}$10) facets. In Fig. 23 (b), (011) facet appears and the dislocations propagated into newly grown crystal intersecting with the facets. The ($\bar{1}$01) facet seems to shrink by dislocation effect (cf. Fig. 21 (c)) but as seen in Fig. 23 (d), growth on the ($\bar{1}$01) facet and (0$\bar{1}$1) facet stops, during the periods of the preferential growth on the ($\bar{1}$10) facet, then the ($\bar{1}$01) facet seems to develop although many dislocations propagate into newly grown crystal, intersecting with the ($\bar{1}$01) facet. The ($\bar{1}$10) facet shrinks (cf. Fig. 23 (d) and Fig. 23 (e), and the (0$\bar{1}$1) facet shrinks as the ($\bar{1}$01) facet keeps stopping.

2. 5. *Dendritic Growth of Single Crystals of* Al-Mg *Alloys*

Most of ingots and castings have a dendrite structure and the fineness of dendrites affects the mechanical properties of the materials. Therefore, numerous investigations have been made both experimentally and theoretically on the mechanisms of the dendrite growth and on the factors which affect the fineness of dendrite structure.

For example, experimental investigations have been made on the transition layer between the dendrite arms,[33,34] the preferred orientation of dendrite arms,[33,35~37] the relationship between supercooling of the melt and growth rate,[33,38] the tip radius of the dendrite arm,[39,46] dendrite arm spacing,[41~45] interface morphology[46,47] and so on. In addition, there have been many theoretical studies

on the dendrite growth, such as the theory of isothermal dendritic growth,[48,49] the theoretical analysis of the primary arm spacing,[50] the theoretical analysis on solute redistribution in dendritic solidification[51] and so on. However, most of the experimental studies of dendrite growth which have been made so far are of the type "ex post facto" to the actual process of solidification.

This is one of the reasons why clarification of dendirite growth mechanism has not yet been obtained. Therefore, direct and real time observation has been much desired.

There have been several reports on real time observations of the solidification process of alloys by optical[52] and electron microscopy.[53,54] However, optical microscopy is not powerful enough to observe microstructures of growing interface of alloys which are not transparent to visual light. Electron microscopy is not suitable for the observation of dendrite growth, in particular, for the determination of the spacing of dendrite arms because of the extreme thinness of the specimen used.

In this study real time X-ray topography, which has already provided us with valuable information on the growth mechanism of pure metals,[55] has been applied to a study of dendrite growth of alloys, and observations have been made in the present experiments on the following subjects;

(1) Continuous observation of growth and morphology of the dendrite arms during solidification as a function of growth rate.

(2) Morphological changes of dendrite arms as a function of Mg content.

(3) Dendrite morphology.

(4) Observations on the morphological changes and solute redistribution during cooling and isothermal annealing after solidification.

(5) Observations of the melting process of previously grown dendrite.

2. 5. 1. Experimental Procedures

In order to avoid possible effects due to size and free surfaces of the specimens in the observation of dendritic solidification by real time x-ray topography, materials with a small μ, where μ is the linear absorption coefficient, and with a relatively low melting point, must be used.

The present observations have been made on aluminum alloys containing 0.5, 2.0, 4.0 and 7.0 at % Mg. The phase diagram of Al-Mg system is illustrated in Fig. 24. Single crystals of these Al-Mg alloys were prepared by strain-anneal method at first. Hot rolled sheets 2 mm thick were cold-rolled into sheets of the size about $200\times20\times1\,mm^3$. These sheets were chemically polished and pre-annealed at 800-870 K for 1.5 hours. Strains ranging from 1 to 5 % were given to these sheets in tension, followed by an annealing just under the melting temperature for 7 hours. The crystallogrphic orientations of the surfaces of the specimen thus prepared and the relationship between the strain and the grain size in the strain-anneal method are shown in Fig. 25. These single crystals were spark-cut into smaller specimens of about $20\times4\,mm^2$, and chemically polished in the solution of 3 parts HNO_3, 19 parts $HClO_4$ and 190 parts CH_3COOH (by volume). The specimens thus obtained had a length of about 20 mm, a width of about 4 mm and a thickness of 0.8 mm.

Using the furnace[17] shown in Fig. 3, processes of unidirectional melting and solidification processes were observed by TV-VTR system. The topographic images were also recorded on Ilford-L4 nuclear research plates, if necessary, to observe

at a higher resolution.

2. 5. 2. Observation of Melting Process

Fig. 26 illustrates TV images of a melting process of Al-4.0 at % Mg crystal after solidification shown in Fig. 27. In this figure, melting proceeds from high-order arms to low-order arms. However, macroscopical melting occurred from upper dendrite arms (located at the part with low temperature). From these results, it can be said that solidification and melting process are not exactly reversed.

Fig. 28 shows the melting process of an Al-4.0at% Mg crystal grown in ⟨100⟩ direction. Melting occurred first in high-order arms (secondary or tertiary arms) located near the tip of the primary arms (Fig. 28 (a), (b)) and melting propagated downward in the high-order arms with increase in temperature (Fig. 28 (c) to (f)). However, in contrast to the melting process of Fig. 26, melting of the primary arms occurred after almost all high-order arms have melted (Fig. 28 (g) to (j)).

2. 5. 3. Interfacial Morphologies as a Function of Growth Rate

Fig. 29 shows morphologies of dendrite in the solid-liquid interface in Al-4.0 at% Mg alloys, recorded on nuclear research plates. In Fig. 29 (a) the growth rate of the primary- or the tertiary arms in the region indicated by A and B were 53 μm/s and 130 μm/s., respectively. In the present study, growth rate means that of the primary arms, unless otherwise indicated. Higher-order (secondary, tertiary, and so forth) arms indicated by the arrows with the respective number can be seen in this figure. Here, "the tertiary arms" mean the arms which grow from the secondary arms and "the quaternary arms" mean the arms which grow from the so-called "tertiary arms", and so forth. In Fig. 29 the secondary and the quaternary arms grew in the same ⟨001⟩ direction and their growth stopped before they impinged on each other. The spacing of the secondary arms of dendrites grown at a low growth rate (region A) is larger than that of more rapidly grown dendrite (region B). This agrees with the results of the conventional "ex post facto" experiments made previously on bulk crystals. Therefore, it may be said that growth conditions in the present study are similar to those of bulk crystals. The morphologies of the secondary or the quaternary arms varied with the change of growth rate. In the larger growth rate region (B), the primary and the secondary arms have made a right angle with each other. On the other hand, they crossed at an acute angle in the region grown slowly (A). In accordance with this, when the crystal was grown at a constant rate, primary and secondary arms crossed at a constant angle throughout the crystal.

Fig. 30 is a series of TV images recorded on a video tape during the solidification with gradual increase in growth rate. Time intervals between each topograph and growth rate for each are indicated below each figure. As shown in Fig. 30 (a) and (c), the secondary arms, which are developed near the tips of the primary arms, are observed to make an acute angle to the primary arms. The angle betwen these secondary arms and the primary arm approached a right angle with the advancement of the tip of the primary arm (Fig. 30 (d) and (e)). On the contrary, if the growth rate became faster (Fig. 30 (f)), the secondary arms extended at an angle nearly equal to a right angle near the growth front.

2. 5. 4. *Morphological Change as a Function of* Mg *Content*

Figs. 31 to Fig. 33 show the effect of change of the growth rate and Mg content on the morphology of the dendrite. Each image was recorded intermittently on nuclear reseach plate with an exposure of 60 seconds during which dendrite growth was interrupted. The angle between the primary and the secondary arms was measured on the topographs. In an Al-4.0at% Mg alloy, the angle between the primary and the secondary arms varied from 72 to 90 degrees with increasing a growth rate from 12 μm/s to 150 μm/s (Fig. 31). The same tendency was observed in an Al-2. 0 at%Mg alloy (Fig. 32) and also in an Al-0. 5 at%Mg alloy (Fig. 33). Furthermore, at the same growth rate of 150 μm/s, the angle between the primary and the secondary arms depended on Mg content; it varied from 90 degrees in an Al-4. 0at%Mg alloy to 69 degrees in Al-0. 5 at%Mg alloy, respectively.

Interrelations among the angle between primary and secondary arms, growth rate and Mg content are indicated in Fig. 34. The observation could not be made on a growth rate faster than 150 μm/s because it was very difficult to interrupt the growth immediately. However, extrapolation shows, for instance, in an Al-0. 5 at% Mg alloy that secondary arms would make a right angle to the primary arms at a growth rate exceeding 200~300 μm/s.

2. 5. 5. *Dendrite Morphologies*

Fig. 35 shows dendrite morphology at the solid-liquid interface of Al-4. 0 at%Mg crystal solidified in ⟨110⟩ direction at a growth rate of 90 μm/s. Fig. 35(a) and (b), recorded on nuclear research plates, were obtained on the same crystal with the interval of 60 seconds. Fig. 35 (b) was taken after rotating the crystal by 0. 05 degrees around the vertical axis relative to Fig. 35 (a).

In crystals grown in ⟨110⟩ direction, the dendrite assembly showed a "V" type structure[56]. These dendrite arms grew along two equivalent ⟨100⟩ directions, making an angle of 45 degrees to the growth direction. No primary arm along ⟨110⟩ was observed and some arms along ⟨100⟩ acted as the primary axis.

Fig. 36 is a series of TV images observed during the solidification process of the same crystal as shown in Fig. 35. From these topographs, the solidification process in ⟨110⟩ direction can be summarized as follows:

(1) Two dendrite arms are generated at the same origin and extended in the two equivalent ⟨100⟩ directions.

(2) These two primary arms grow preferentially and are accompanied by an upward growth of secondary arms (Fig. 36).

(3) Secondary arms grow upward at a slow speed making right angles with the primary arms.

(4) Preferential growth of one of these secondary arms occurs.

(5) The secondary arm acts like the primary arm and the processes described in (1) to (4) are repeated. The process mentioned above is illustrated schematically in Fig. 35.

Dendrite morphology near the solid-liquid interface during solidification approximately in ⟨111⟩ direction is shown in Fig. 37. These images are recorded on nuclear research plates with a short interruption of growth. In this case, three primary arms should grow in the three equivalent ⟨100⟩ directions making an angle of 54. 7 degrees to the growth direction. However, only one of these arms was observed to grow preferentially; this can be attributed to a slight deviation of growth direction from the intended growth direction.

Fig. 38 shows dendrite morphology of Al-0.5 at%Mg crystal during growth in ⟨130⟩ direction at a growth rate of 40 μm/s and 10 μm/s, and well-defined primary arms were observed to grow in ⟨100⟩ direction.

2. 5. 6. Morphological Changes of Dendrite Arms as a Function of Growth Rate and Mg Content

The present real time X-ray topographic observations show that the angle between the primary and the secondary arms is not necessarily a right angle but depends on the growth rate and Mg concentration (Fig. 29 and Fig. 31 to Fig. 33).

Paramenters which may affect the growth rate of the secondary arms will be discussed, based on the results of the present study and those of the conventional "ex post facto" studies as follows:

(1) Tip radius of the primary arms

The tip radius decreases with an increase of the growth rate[57], namely, the tip radius at a low growth rate (e. g., Fig. 31(a)) is larger than that at a high growth rate (Fig. 31(c)). The secondary arms generate and extend so as to minimize the surface energy, i. e., they make a right angle to the surface of primary arms. Therefore, if the secondary arms are generated at the tip of the primary arms, it is possible for the primary and the secondary arms to make an acute angle at a low growth rate. However, it has been pointed out[58] that the distance between the tip of the primary arm and the location at which the secondary arms are generated increases with the increase of the tip radius. Consequently, the tip radius is unlikely to affect the angle between primary and secondary arms.

(2) Temperature gradient in the system

The temperature gradient used in the present observations is about 1.0 K/mm, which is quite small compared with that used in the conventional studies.

In the case of dendrite growth under a small temperature gradient, a relatively extensive region in the melt near the solid-liquid interface may be undercooled. If the secondary arms are generated at an acute angle with the primary arms for some reason, they can grow in the direction which makes an acute angle with the primary arm because of the existence of an undercooled region. When the temperature gradient is large near the tip of primary arms, these secondary arms could not extend upward because of the increasing temperature along this direction.

Consequently, the temperature gradient near the tip of primary arms is responsible for the observed morphology of secondary arms.

(3) Concentration of Mg in the dendrite arms

In the case of rapid growth, the concentration of Mg in the liquid near the solid-liquid interface became high because Mg was exhausted from dendrite arms, and could not diffuse sufficiently into the liquid due to lack of time for diffusion. On the contrary, in the growth at a small rate, the concentration of Mg in the growing dendrite arms approaches the equilibrium concentration. From the observations shown in Fig. 33 the angle between the primary and the secondary arms approaches a right angle as the macroscopical growth rate increases. Therefore, it can be said that the angle between the primary and the secondary arms depends on the concentration of Mg in the growing dendrite arms. This speculation is in agreement with the experimental result that the angle is proportional to the initial Mg content in the bulk crystal.

Consequently, the generation of secondary arms which make an acute angle with the primary arms relates to the concentration of Mg in the growing dendrite

arms.

Concentration profiles of Mg

From the observations of the melting process, Mg content at different parts of the dendrite arms have been estimated. According to the phase diagram of Al-Mg system, the melting temperature decreases with increasing Mg content in the range of concentration studied in the present study.

In ⟨100⟩ direction growth, the melting occurred at first in the high-order dendrite arms. After most of these arms had been melted, the primary arms began to melt from tip to lower part. This indicates that there is a considerable difference in the concentration of Mg between the primary arms and the other high-order arms.

The concentration profiles of Mg in columnar dendrite are estimated from these observations and illustrated schematically in Fig. 39. This profile obtained just after the solidification differs from the experimental concentration profiles obtained at room temperature with "ex post facto" method.

2. 6. Discussion

2. 6. 1. Microscopical Structure of the Solid-Liquid Interface of Aluminum and Gallium during Crystallization

From the observations of interfacial morphology during the growth process and the effect of dislocations on the morphology of a growing interface, the atomic structure of solid-liquid interface will be discussed, and compared with the theoretical expectations.

Jackson[25~27] introduced the concept of roughness and classified the roughness of the interface of materials into two categories, that is, smooth interface and rough one, using the two-dimensional Ising model.

Temkin[43] proposed the concept of diffuseness of the interface on the basis of a multilayer model which was an expansion of Jackson's two-level model.

Cahn used a continuous model to describe the interface.[35] According to his theory, the surface energy of an interface depends on the mean position of the interface with respect to the atomic plane, and therefore, the surface energy should vary periodically as the interface moves.

The solid-liquid interface of aluminum during the growth was observed to lie along the isothermal plane of the crystal throughout the observations (Figs. 14 to 16) and no faceting of the growing interface was observed even in the case of growth under a low temperature gradient (1.0 K/mm), as is shown in Fig. 15. Furthermore, the morphology of the interface never changed by the intersection of dislocations with the interface. From this, the solid-liquid interface of aluminum should be "rough" in terms of Jackson's roughness (because α for Al is less than 2), or "diffuse" in terms of Temkin's diffuseness (cf. Table 3)

Table 3. Jackson's parameter α of aluminum and gallium crystals.

	habit plane	Jackson's parameter α
aluminum	all	$\alpha<2$
gallium	(010)	$\alpha>2$
	the others	$\alpha<2$

With respect to Cahn's theory, neither growth by lateral mechanism nor by transitional mechanism, which are predicted in his theory, has been observed within

the range of temperature gradient and the supercooling obtained in the present study.

In the case of gallium, (010), (110), (011) and (111) facets were observed at the solid-liquid interface during growth (Fig. 21-Fig. 23). The solid-liquid interface in gallium on atomic scale ought to be "smooth" in Jackson's term and "sharp or diffuse one with steps" in Temkin's term. These types of interface are schematically illustrated in Fig. 40.

If the surface structure of the observed (010), (110), (011) and (111) facets was the smooth interface expected from the Jackson's theory, these facets should advance and reduce in size when they intersect with screw dislocations. However, the bundles of dislocations with different Burger's vector did not affect the faceted growth as shown in the Fig. 22. It is very unlikely that all the dislocations belonging to this bundle are of edge character, which does not affect the growth rate of a facet. Furthermore, many facets such as (110), (011) and (111) are not expected to appear from Jackson's theory because the Jackson's α parameter for these facets is 1.12 (cf. Fig. 21 to Fig. 23).

One possible explanation of the latter discrepancy is to modify Jackson's α parameter by considering the second nearest neighbor atoms, as follows:
For gallium,

$$L/kT_m=2.24$$

where L is latent heat of melting, k Boltzman's constant and T_m melting point in kelvin. When the first nearest neighbor atoms are considered, $\eta_1=2$ for (110) and (011) plane. However, the distances to the first nearest neighbor atoms and to the second nearest neighbor atoms in (110) plane are 4.42 and 4.45, respectively, and almost the same. If the first and the second nearest atoms are taken into consideration, (therefore, $\eta_1=4$), α is calcuated as follows,

$$\alpha=(L/kT_m)(\eta_1/\nu)=2.24$$

where ν is coordination number and $\nu=4$ in the present case, η_1 the number of nearest neighbor atoms on a habit plane. In this case, (110) surface should be smooth and (110) facet should appear, since α for (110) becomes larger than 2. Thus, facetedgrowth observed on (110), (011) and (111) in Fig. 21-Fig. 23 can be explained by modifyng Jackson's theory.

With respect to Temkin's theory, sharp interface can be related to the faceted growth when the crystal surface in contact with its melt is smooth. Furthermore, the fact that the (011) facet observed in Fig. 23 stopped advancing to gain the supercooling necessary for a further growth denies the possibility of growth on the Temkin's diffuse interface with steps.

Therefore, Jackson's theory is of general validity for the faceted growth of gallium. However, in details, Jackson's theory is in conflict with the experimental result that dislocations observed in Fig. 21 and Fig. 23 do not affect the faceted growth. Some further modification of the theory is hoped.

With respect to Cahn's theory, a major disadvantage of this theory is that curve-fitting is the only way to determine the diffuseness of the interface. In the present study, the breaks from lateral growth kinetics to continuous growth kinetics, which are expected from his theory, have not been observed. Therefore, his theory

can not be applied to the present findings.

2. 6. 2. Mechanisms of Crystal Growth from the Melt of Aluminum and Gallium

From the result of observations of the solid-liquid interface during growth and the discussion on the microscopical structure of the solid-liquid interface mentioned above, the mechanism of crystal growth of aluminum from the melt will be discussed here.

The solid-liquid interface of aluminum always lies along the isothermal plane of the crystal and advances normal to the isothermal plane of the system. Therefore, it can be said that the growth of aluminum crystals is isotropic. Consequently, the growth of aluminum is expected to be a continuous growth or an adhesive growth. Moreover, since the microscopical structure of the interface of aluminum is likely to be rough or diffuse, a crystal growth of aluminum is considered to be continuous or adhesive growth.

Now let us infer the growth mechanism from the result of real-time observation of faceted growth of gallium. According to the theories of Jackson and Temkin, macroscopic faceting of the interface is formed by growth rate anisotoropy. In a range of the temperature gradient employed in the present experiment, anisotropic growth implies that the growth is governed by a lateral growth mechanism.

In Fig. 23 (b) to (d), $(\bar{1}01)$ facet which is in the center of the solid-liquid interface repeats shrinking and spreading in turn as the crystal grows. This is illustrated schematically in Fig. 41. In this case, it is supposed that a preferencial nucleation occurs at the center facet ($(\bar{1}01)$ facet) resulting in a preferential growth of the center facet (Fig. 41(a)); the center facet appears as if it shrank, as seen in Fig. 23 (c). Because of the latent heat generated at this facet as a result of preferential growth, this facet can not gain a supercooling necessary for a further growth. Therefore, growth on this facet stops (see Fig. 23 (d)). During this process, growth on the $(0\bar{1}1)$ and $(\bar{1}10)$ facets which are located on the either sides of $(\bar{1}01)$ facet keeps stopping. This indicates that the rate of lateral spread of nuclei is low; it is almost same as the rate of nucleation.

On the contrary, if the nuclei spreads rapidly compared with the nucleation on facets as shown in Fig. 41 (b), the nuclei would spread from the edges of the center facet (A, B) to the side facets and the growth would also occur at these side-facets at a speed almost the same as that of the center facet.

From this, it is concluded that gallium crystals grow by lateral mechanism on smooth interface, and that the rate of lateral spread of nuclei is almost the same as the rate of two-dimensional nucleation on the surface. This conclusion is favorable to the Jackson' theory.

Kinetic experiment on the growth of aluminum

According to the theoretical predictions by Jackson and Temkin based on the lattice model of the melt, growth rate anisotropy on the adhesive growth should not be observed in aluminum. Computer experiment on the kinetics of growth from the melt of f. c. c. metals shows that growth on the rough interface should be isotropic. However, the difference of growth on (110) and (111) is observed in Fig. 18. This growth rate anisotropy, which was not expected from the theories for the growth of aluminum from the melt, indicates that the mechanism of growth from the melt can not always be predicted by these theories.

In summary, real-time observations of the growth processes of aluminum and gallium single crystals have been carried out using x-ray topography. The microscopical structures of the solid-liquid interface and mechanisms of growth from the melt of aluminum and gallium are clarified as follows;

(1) The solid-liquid interface of aluminum during growth is likely to be rough.
(2) The growth of aluminum is continuous growth.
(3) The solid-liquid interface of gallium during growth is smooth.
(4) The growth of gallium is lateral growth and the rate of lateral spread of nuclei is almost the same as that of nucleation.
(5) These results are favorable to the Jackson's theory, although it needs partial modification.

Discussion on melting process

In the x-ray topographs taken during the melting process of aluminum shown in Fig. 11 and Fig. 12, no intensity enhancement was observed in the vicinity of the interface. In the cases shown in Fig. 11 and Fig. 12, the reflecting planes used were nearly perpendicular to the solid-liquid interface. By taking into account the criterion that topographic images show no contrast for the reflecting plane to which the displacement of atoms is parallel, there is a possibility that we cannot detect the distorsion perpendicular to the interface in Fig. 11 and Fig. 12. However, in the observation of melting process shown in Fig. 13, the reflecting plane was nearly parallel to the solid-liquid interface, and no intensity enhancement was observed in the vicinity of the interface. Consequently, there is little lattice distorsion in the aluminum crystal near the interface within the limit of resolution of the x-ray topographic imaging system, (in spite of existence of volume change between the liquid and the solid).

In the observations mentioned above, no equal-thickness fringe was observed near the solid-liquid interface. From this, it can be said that the crystal surface in contact with its melt was nearly planar and that the temperature gradient in the crystal was almost completely unidirectional. Therefore, we can relate the morphological changes, which should appear during growth, directly to the mechanism of crystal growth.

The continuous observations mentioned above also showed that dislocations introduced during the temperature rise up to the melting point did not move until they came into contact with the liquid interface, and no intensity enhancement was observed in the vicinity of the interface.

This observation conflicts with the results observed on Si and Sn. According to the observations during the growth process of aluminum, however, dislocations in the region of high perfection may be detected, if any, within the resolution of the imaging system used in the present experiment, which is not so good as that used by Chikawa et al. and Nittono et al. This can be explained by considering that the thermal stress caused by temperature gradient in the crystal (1.0 K/mm to 10 K/mm) heated by the furnaces was too small to move dislocations.

The lattice distorsion near the interface and the behavior of dislocations in gallium crystal were similar to that of aluminum. The volume change of gallium crystals at the melting point is negative, although that of aluminum crystals is positive. In spite of this, the results of observations on the lattice distorsion and the behavior of dislocations during melting process are almost the same to aluminum and gallium.

3. Origins of Dislocations Introduced during Crystal Growth

3. 1. Introduction

The growth of dislocation-free or low dislocation density single crystals has been of great interest because such crystals have been required not only for basic research on crystal characteristics but also in semiconductor technology. The preparation of dislocation-free crystals of silicon and germanium has played an essential role in both physics and technology of semiconductor.

In the crystal growth from the melt, the following three processes must be considered as extrinsic origins of dislocations.

(1) Propagation of pre-existing dislocations into the growing crystal from the seed crystal.

(2) Generation of dislocations due to segregation of solute atoms or impurities.

(3) Generation of dislocations by thermal stress and/or mechanical interaction of a crystal with the crucible walls when the crystal is grown in a crucible.

Besides these extrinsic processes, the following two models have been proposed as the intrinsic origin of dislocations.

(4) Inheritance of dislocations from the liquid state which can be modelled as a coagulation of a large number of dislocations.

(5) Transformation of vacancy clusters, which are formed by excess vacancy condensation into dislocation loops.

According to the vacancy condensation mechanism, it is assumed that the initial vacancy concentration is equal to the equilibrium value at the melting-point. Any excess vacancies arising from a temperature decrease will condense, in many cases, on the atomic planes to form vacancy clusters or discs. The formation of dislocation loops from these clusters of vacancies will occur as long as the excess free energy associated with formation of dislocation loops is less than that for the clusters.

Dislocation models of the liquid state have been developed by Mizushima,[59] Ookawa,[60] Kuhlmann-Wilsdorf et al.,[61,62] Cotterill et al.,[63] and Suzuki[64] and growth theories based on these models have been put forward. In Ookawa's theory, for example, it was assumed that a free energy barrier between the liquid and the solid phase can be easily surmounted without the aid of the thermal activation when a supercooling exists. Although the dislocation density decreases in the solidification process, part of the dislocations in the liquid phase are inherited into the solid phase. The number of these inherited dislocations will decrease in a short time, resulting in a decrease of free energy in the solid phase. Ookawa calculated the change in dislocation density as a function of time, and concluded that dislocations of density of about 10^3 cm/cm^3 inevitably remain in a bulk solid phase of ordinary metals such as Al and Cu under usual experimental growth conditions.

The most suitable experimental method to investigate how dislocations are introduced into a growing crystal is in-situ observations of dislocations near the solid-liquid interface during the growth process of a crystal and the cooling process after solidification.

3. 2. Experimental Procedures

The method of real time observations of the process of crystal growth by x-

ray topography using a 90 kW-class rotating anode X-ray generator has been described in detail previously (Chapter 2. 3). Single crystals of aluminum (5N) were prepared by the strain-anneal method and single crystals of gallium (6N) with low dislocation density were grown by the Bridgman method. These single crystals were cut into small pieces with a size of about 30×5 mm^2. The thickness of these specimens was 0. 7 mm for the aluminum crystals and 0. 1 mm for the gallium crystals.

The temperature gradient in the specimen was about 1. 0 K/mm for aluminum near its melting point (933 K) and 0. 4 K/mm for gallium. Because of a relatively low yield stress of metallic materials at elevated temperatures, dislocations in metal crystals are very sensitive to the thermal stress and move very easily by a small fluctuation of temperature. Therefore, it was difficult to record the images of dislocations at high temperatures on a nuclear research plate, since in the ordinary experimental conditions the exposure time necessary for recording dislocation images is about 100 s. For this reason, the x-ray topographic observations were made mainly using an x-ray sensing TV camera.

Since the signal-to-noise ratio (S/N) of a single frame image (30 frames/sec) was not high enough to observe individual dislocations in the aluminium crystal, 8 to 32 TV frames were superimposed to improve the S/N ratio: the averaging of n TV frames improves the S/N ratio by a factor $(2n-1)^{1/2}$. This superimposition of 8 to 32 frames needs 0. 27 to 1. 1 s, so that it was necessary to grow the crystals at a rate slow enough. Therefore, the growth rate used in the present experiments was in the range of about 5 to 50 μm/s.

3. 3. Experimental Results

3. 3. 1. Dislocation Behavior near the Solid-Liquid Interface of Aluminum during Crystal Growth

Fig. 42 is a series of x-ray topographs taken during the growth process of aluminum (32 TV frames superimposed). The growth rate was 9 μm/s and the temperature gradient in the crystal near the solid-liquid interface was 1 K/mm. A straight and oblique line which intersects with the interface is an image of a subboundary, which was inherited from a seed crystal and propagated into the newly grown crystal. The lower part of the crystal appears black due to the existence of many dislocations which were generated during cooling after solidification. But, in a region adjacent to the interface no dislocation is seen (Fig. 42 (a)).

This dislocation-free region, 1 mm in width as is indicated by arrows, followed the interface, as seen in Fig. 42 (b), keeping its width unchanged. Many dislocations were generated behind this dislocation-free region. This is also seen in Fig. 42 (c), and again, the width of the dislocation-free region remained unchanged.

To observe the configuration of dislocations in the newly grown crystal region in more detail, topographic images were recorded on Ilford-L4 nuclear researeh plates. Fig. 43 (a) to (c) show TV images of x-ray topographs during the melting and growth processes and Fig. 43 (d) and (e) are the magnified images of the area indicated in Fig. 43 (a) and (c), recorded on nuclear research plates just before melting and just after growth, respectively. Comparison of Fig. 43 (d) with (e) showed that a newly grown crystal is highly perfect just after growth, perhaps except for the presence of point defects, which cannot be resolved. In Fig. 43 (b), some vague images are seen. These are dislocations introduced after growth by

mechanical interaction with oxide film formed on the surface of the crystal. Therefore, it can be concluded that there is a region of high perfection (most probably dislocation-free) in the crystal adjacent to the solid-liquid interface during growth.

To investigate the effect of the growth rate on the perfection of crystals, the growth rate was suddenly changed during the growth process. Fig. 44 shows the process in which many dislocations were generated by a change of growth rate. These images are produced by averaging 8 TV frames. Broad linear images are a bundle of many dislocations. Fig. 44 (a) is a topograph taken just before the change of growth rate, the previous growth rate being 20 μm/mm. The growth rate between fig. 44 (b) and (d) was 42μm/mm. After changing the growth rate from 20 μm/mm to 42 μm/mm, the pre-existing dislocation bundle thickened; many dislocations were generated from the pre-existing dislocation bundle. However, it is to be noted that just after the change of the growth rate (Fig. 44 (b)), the generation of dislocations was not yet observed in those regions which were distant from the dislocation bundle; it is not until the interface advanced farther that many dislocations were suddenly generated in the whole area of the crystal which had been grown after the change of growth rate (Fig. 44 (c)). Subsequently, the number of dislocations increased. In this case again, the region adjacent to the solid-liquid interface remained dislocation-free except in the vicinity of the pre-existing dislocation bundle, as seen in Fig. 44 (d).

Thus, an increase in growth rate results in an increase in dislocation density, but this increase occurs in the crystal which is well behind the solid-liquid interface.

3. 3. 2. Dislocation Behavior in Aluminum during Cooling after Solidification

Fig. 45 shows the propagation of dislocations during cooling just after the solidification of Fig. 42. The temperature of the top of the crystal was 931 K and 928 K in Fig. 45 (a) and (b), respectively. The cooling rate was about 5 K/hr., and the temperature gradient of the crystal was 1 K/mm. During cooling many dislocations were generated from the bottom (the region of lower temperature) to the top (the region of higher temperature) of the crystal. At the same time, part of these dislocations multiplied themselves and coalesced into a bundle of dislocations, as can be seen in Fig. 45 (b).

Fig. 46 is a series of topographs taken on the same specimen during further cooling after Fig. 45 had been taken. The temperature of the specimen was indicated in the figures. The cooling rate between (a) and (b) was 12 K/hr, and the time interval between (b) and (c) was 2 hours. On further cooling, multiplication of dislocations continued, as shown in Fig. 46 (a) and (b). At the same time, sub-boundaries were formed gradually during isothermal annealing between Fig. 46 (b) and (c) with the perfection of the inside of sub-boubdaries being improved. From these observations it may be concluded that two different phenomena take place during cooling; one is the multiplication of dislocations arising from a decrease of temperature and the other is a change of configuration of dislocations into dislocation bundle or sub-boundaries which is to be attributed to thermal annealing.

3. 3. 3. Dislocation Behavior near the Solid-Liquid Interface of Gallium during Crystal Growth

Fig. 47 shows a series of enhanced TV images of topographs taken during a growth process of gallium single crystal. The solid-liquid interface is faceted along (110) and (111) crystallographic planes. The growth rate of these facets was about 3 μm/sec. In this case, the seed crystal was highly perfect and no dislocations were observed to propagate from the seed crystal, as can be seen in Fig. 47 (a). Furthermore, no dislocations were observed to be generated over the whole crystal during the subsequent growth (Fig. 47(b) and (c)). In another observation where the seed crystal had some dislocations (Figs. 21 to 23) no dislocations other than those propagating from the seed crystal were observed.

Consequently, it can be concluded that dislocation-free single crystal of gallium can be grown under a proper growth condition.

3. 4. Discussion

In the topographs shown in Figs. 42 to 46 no evidence of individual dislocations was obtained. Although the resolving power of the TV imaging system employed is not so good as that of nuclear research plate, in view of that a generation or multiplication of bundles of dislocation during growth and cooling processes could be observed successfully using an image processor, it may be concluded that gallium crystals grown at a slow rate (less than about 40 μm/s in the present study) are actually free from at least dislocation bundles and, most probably isolated dislocations.

As is already mentioned in 3. 1, possible origins of dislocations during growth and cooling process of a metal crystal can be classified into two groups, i. e., the intrinsic ones and extrinsic ones. They may be summarized as follows.

Extrinsic origins:

(1) Propagation of pre-existing dislocations from the seed.

(2) Generation of dislocations due to the segregation of solute atoms and/or impurities.

(3) Generation of dislocations due to a thermal stress.

Intrinsic origins:

(4) Inheritance of dislocations from the liquid state itself.

(5) Condensation of vacancies

In the present observations described above, no evidence of the extrinsic origins of dislocations ((1)-(3)) were obtained. Thus, we can concentrate on the intrinsic origins ((4) and (5)), and these will be discussed in some more details' in the following.

Dislocation inheritance from the liquid

Dislocations are considered as being inherited from the liquid, which is modelled as a coagulation of a large number of dislocations.

The formation mechanism of dislocations based on the liquid structure has been put forward by Ookawa. His calculation showed that in a practical time scale of growing and annealing of a cryatal, dislocation of at least about 10^3 cm/cm^3 remain inevitably in the crystal. This result conflicts with the present observations that a crystal near the growing interface is free from dislocations (Fig. 42).

Suzuki[64] proposed that, under a small supercooling phase separation with

respect to the dislocation density must occur in the solid-liquid interface, that is, the dislocation-free phase (solid phase) and the dislocation-containing one (liquid phase) can coexist stably. The density of dislocations changes stepwise at the interface from zero to the density of the liquid. Therefore, a crystal always grows without accompanying dislocations. This prediction is in good agreement with the present observation (Fig. 42) in the sense that a dislocation-free region exists near the interface. However, Suzuki's theory cannot explain the experimental fact that a slight increase in growth rate results in the generation of dislocations in the crystal (cf. Figs. 44).

According to Kamada[65] the dislocation generation can be explained by a dislocation model based on Cotterill's theory. Cotterill believed that dislocations in the interface escape to the bulk melt, and that a crystal grows without accompanying dislocations. Excess dislocations annihilate with each other to keep the thermal equilibrium density of the bulk melt. This mutual annihilation of dislocations produce the latent heat of solidificatioin. Based on these assumptions, Kamada evaluated the velocity with which a dislocation escapes out of the interface into the bulk melt and concluded that this theoretically derived dislocation velocity is in agreement with the observed upper limit of the growth rate needed for dislocation-free growth. Therefore, Kamada's hypothesis predicts that if the growth rate of crystals exceeds the aforementioned characteristic growth rate, dislocations should be generated at the interface. This is in good agreement with the present observation. However, Kamada's prediction cannot explain the observed result that there is an incubation period in the generation of dislocations during growth (Fig. 44). The same difficulty applies also to Suzuki's theory.

Vacancy condensation

The other model is based on collapsing of vacancy discs which are formed by condensation of excess vacancies. If dislocations are introduced by the vacancy condensation mechanism, no dislocations should be observed in the crystal adjacent to the solid-liquid interface, because some degree of undercooling is necessary to obtain the excess concentration of vacancies required to form vacancy discs or dislocation loops. However, there have been criticisms against this type of theories.

For instance, Schoeck and Tiller[66] assumed that any excess concentration of vacancies arises solely from a temperature change and that the initial vacancy concentration is the equilibrium value at the melting point. However, this equilibrium concentration of vacancy cannot explain the observed density of the vacancy discs or dislocation loops. There have been arguments against this theory. Much higher supersaturation of vacancy must be assumed in order to explain the observed density of vacancy discs or dislocation loop.

Bolling and Fainstein[67] tried to modify Schoek and Tiller's theory by invoking a trapping of vacanceis by the interface. They assumed a diffuse interface proposed by Temkin and concluded that if vacancies contained in the liquid are trapped by the solid-liquid interface which is advancing into the crystal, defects due to excess vacancies could be formed at high temperatures. This theory can explain the observation that an increase in the growth rate results in an increase in the dislocation density, because an increase in the growth rate will result in an increase in the number of those vacancies that are trapped by the interface.

Therefore, it can be concluded that the present observations support the vacancy condensation mechanism of Bolling and Fainstein, although actual number of excess

vacancies trapped at the advancing interface may be greater than estimated by them, because many dislocations are generated during growth as shown in Fig. 44.

This vacancy trapping may occur in order to compensate the difference in the density between the liquid and the solid. In an ordinary metal such as aluminum the density of the liquid is smaller than that of the solid. In other words, the liquid of such metal will contain more vacancies than the solid. Therefore, it may be presumed that many vacancies are trapped at a solid-liquid interface advancing into the liquid. Thus, dislocations are likely to be generated during growth by vacancy condensation.

On the other hand, in materials such as silicon and gallium the density of the liquid is greater than that of the solid. Therefore, less vacanceis will be trapped by the solid-liquid interface than in an ordinary metal. This may explain the reason why crystals with higher perfection may be obtained in these materials than in ordinary metals. However, it is needless to say that this presumption must be confirmed by experiment on other metallic materials such as bismuth and antimony whose density in liquid state is smaller than that in solid state.

Moreover, according to the present presumption, in order for crystals with high perfection to grow some growth conditions such that crystals should be thin and the temperature gradient should be small must be satisfied.

Summary

Real-time x-ray topographic observation of crystal growth of aluminium from the melt showed that a dislocation-free solid region exists near the solid-liquid interface. When the growth rate exceeds a certain value, say 40 μm/sec in the present experiment, many dislocations were observed to be generated, but with some incubation time.

In the growth of gallium single crystal from a highly perfect seed no dislocations were observed to be generated over the whole area of crystal under growth conditions employed in the present study.

From these observations, it is concluded that the most probable origin of dislocations associated with crystal growth is vacancy condensation, and also that unit process of crystal growth from the melt is likely to be "atom by atom" process or similar ones.

The present observations show that growth theories based on the dislocation models of liquid state are of doubtful validity.

4. Morphological and Microstructural Changes After Solidification

4. 1. *Dislocation Behavor in Pure Aluminum during Cooling after Solidification*

Fig. 45 shows the propagation of dislocations during cooling just after solidification shown in Fig. 42. Each image is enhanced by an image processer. The temperature of the top of the crystal was 931 and 928 K in Fig. 45 (a) and (b), respectively. The cooling rate was about 5 K/hr and the temperature gradient of the crystal was 1 K/mm. On cooling, many dislocations were generated, which pro-

pagated from the bottom (lower temperature) to the top (higher temperature) of the crystal with multiplication taking place. At the same time part of these dislocations were observed to coalesce into a bundle (Fig. 45 (b)).

Fig. 46 is a series of topographs taken on the same specimen during further cooling from 924 to 920 K after Fig. 45 had been taken, the cooling rate between (a) and (b) being 12 K/h. The specimen was held at 920 K for 2 hours between (b) and (c). On further cooling, multilication of dislocations took place more and more frequently, as is shown in Fig. 46 (a) (b). On the other hand, during isothermal annealing between (b) and (c) subboundaries were formed gradually, with the perfection inside the subgrains being improved. These observations show clearly that the multiplication of dislocations takes place while a crystal is being cooled after solidification and that coalescence of dislocation into bundles or subboundaries is attributed to an annealing effect.

4. 2. *Morphological Changes of Dendrites in Aluminum-Magnesium Alloys during Cooling and Isothermal Annealing after Solidification*

Morphological changes of dendrites in Al-Mg alloys during cooling and isothermal annealing were also observed. Topographs shown here were recorded on nuclear research plates except for Fig. 36.

Fig. 48 shows a change of dendrite structure of Al-4.0 at.% Mg alloy crystal cooled at a relatively slow rate after solidification. In Fig. 48 (a) it was observed that the primary, the secondary and the tertiary arms crossed each other perpendicularly. When a crystal is cooled slowly enough after solidification, the dendrite morphology changes gradually only to a small extent. Especially as long as the crystal was cooled within 10 K of the melting temperature, little change in dendrite morphology was observed, although, on further cooling, some gradual change was observed. These changes are to be attributed to a change in the lattice constant. That is, thermal expansion is responsible for the gradual change in dendtrie morphology observed during slow cooling.

On the other hand, a more drastic morphological change took place during a more rapid cooling. Fig. 49 shows a series of x-ray topographs, reproduced from TV images, of a growth process ((a)～(d)) and subsequent cooling at a rate of 1 K/s ((e)～(h)). In Fig. 49 (c) a distortion of a dendrite arm took place at the location indicated by arrow, and then further distortions took place at other locations ((d) to (f)). In Fig. 49 (g) and (h), a rapid change in dendrite morphology took place over the whole area of the crystal. Those distortions are considered as being due to a shrinkage at the crystal surface, while that shown in Fig. 49 (g) and (h) may be attributed to a stress which arises from the segregation of Mg. The lattice distortion of each dendrite arm in the former case is estimated to be about $\pm 0.3°$ from another observation (not shown).

Fig. 50 shows effect of isothermal annealing near the melting point on the morphology of dendrite. Fig. 50 (a) was taken just after the growth of the dendrite arms. On annealing isothermally for 3 minutes, the primary arms became thick presumably by absorbing molten metal and/or the secondary arms. However, further annealing for 18 minutes at 657 K brought out little change in dendrite morphology.

During isothermal annealing at lower temperature, say 100 K below the melting point, little change was observed in morphology of dendrite, as is shown in Fig. 51.

Therefore, it can be concluded that a morphological change of dendrite arms

during isothermal annealing takes place very quickly in the first few minutes only when annealed near the melting point.

4. 3. Discussion

Rapid change in dendrite morphology was observed during growth and subsequent cooling at a relatively high cooling rate of 1 K/s. In the first stage lattice distortion of dendrite arms takes place, which may be attributed to a stress generated by shrinkage of the crystal. The subsequent change in dendrite morphology, which took place over the whole area of the crystal may be attributed to the internal stress which originates from the segregation of Mg.

The morphological change in dendrite arm takes place during isothermal annealing near the melting point. In this case, the primary arms seem to thicken by absorbing the secondary arms. This morphological change took place only during the first stage of annealing. It is concluded that this type of morphological change is controlled by diffusion of solute atoms into the solid.

In conclusion, it may be said that the conventional method of observation of morphology of dendrite, which is carried out after solidification, may not give information about the morphology of dendrite during or just after the solidification, which is of vital importance to understand the mechanism of the formation and growth of dendrites. This is one of the greatest advantages of real-time x-ray topographic study of solidification of alloys over the conventional method.

5. Thermal Cyclic Annealing and Improvement of Crystal Perfection

5. 1. Introduction

Highly perfect crystals with low dislocation density and very few subboundaries are greatly desired in various fields of solid state physics such as diffraction physics and crystal plasticity. Several techniques have been developed to obtain such highly perfect crystals. These techniques can be classsified into two groups. In one, highly perfect single crystals are obtained by controlling the condition under which single crystals are grown either from melt or from strained polycrystals. In the other, as-grown single crystals are relatively imperfect, but the perfection is improved by subsequent annealing in solid state at elevated temperature (after growth of single crystals). Kitajima et al.[68,69] have found that thermal cyclic annealing is much more effective in reducing the densities of both dislocations and subboubdaries in Cu than the conventional isothermal annealing. In this chapter the thermal cyclic annealing technique has been applied to a variety of materials with different crystal structures in order to test whether or not the thermal cyclic annealing technique is of universal use in improving crystal perfection.[70,71,72]

5. 2. Specimens and Procedures

Specimens used in this study are pure Ag, Ag-In, Ag-Sn, Ag-Sb alloys (fcc), Si (diamond) and Fe-3%Si alloy (bcc) single crystals. Single crystals of Ag and its alloys were grown by the Bridgman technique, and those of Si were by floating zone-melting technique, while those of Fe-3 % Si alloy were grown by the strain-annealing technique.

The thermal cyclic annealing was carried out either in vacuum or in a Ti-

gettered argon atmosphere by varying the temperature of the furnaces in such a way that the maximum temperature is just below the melting point of the material being annealed and the minimum temperature is lower than the melting point by about 200℃. A typical example of temperature variation at a point on the specimen surface during the thermal cyclic annealing is shown in Fig. 52.

The perfection of the crystals annealed thermo-cyclically was characterized either by etch-pit method (for Ag and its alloys) or by X-ray topographic method (Si and Fe-Si).

5. 3. Results

5. 3. 1. Ag and its Alloys

The dislocation densities of the as-grown crystals are determined as a function of solute content after removing the layer of about 0. 2mm in thickness from the as-grown surface by chemical polishing. This procedure eliminates the layer near the as-grown surface which has a slilghtly higher dislocation density than in the interior of the crystal.

Fig. 53 shows the effect of Sn content on the dislocation density of as-grown crystals. The dislocation density ranged from 2×10^4 to $3\times10^5/cm^2$ and there is no systematic correlation between the solute content and the dislocation density in the range of tin content studied. This result is in good agreement with those by Hammer,[73] except that the dislocation density of Ag alloys grown by Hammer et al. is higher approximately by two orders of magnitude ($1\times10^6-1\times10^7$). It is also confirmed that the crystals prepared in the present study do not contain subboundaries. Effect of solute addition on the dislocation configuration is small in the range of Sn content up to 0. 73 at.%. However, in crystals with higher solute contents well-developed subboundaries were often observed. Similar results were obtained in the other Ag alloys.

It was reported that isothermal annealing at 940℃ for two weeks reduced the dislocation density of pure Ag from $(1-5)\times10^6$ in the as-grown state to about $5\times10^4/cm^2$. In the present study, both isothermal and thermal cyclic annealing were applied to Ag and its alloys. The relations between dislocation density and annealing time are summarized in Fig. 54 for both pure Ag and Ag-Sn alloys. Thermal cyclic annealing is more effective in reducing the dislocation density than isothermal annealing at 940℃. This is true for all the other Ag alloys studied.

5. 3. 2. Fe-3 % Si

Fig. 55 (a) shows a typical x-ray topograph of an as-grown single crystal. The crystal contained many elongated subgrains whose shorter diameter ranged from 1 mm to 2 mm, and the crystals inside the subgrains contained many dislocations as well. After annealing the as-grown single crystal isothermally for 56 hours (Fig. 55 (b)), the subgrains grew to as large as 5 mm and the perfection inside the subgrain was improved profoundly. However, the subboundaries did not disappear completely.

Fig. 56 (a) (b) shows similar x-ray topographs but taken on a specimen annealed for 20 hours thermo-cyclically. It is evident that subboundaries disappeared completely, and that the crystal contained very few dislocations.

Perfection of the crystal was also assessed by measuring the half-width value of the rocking curve. Fig. 57 shows an example of the rocking curve of 110 reflec-

tion obtained using the single crystals that were annealed thermo-cyclically for 60 hours. Rocking curve thus obtained shows that the half-width value is as small as 13 seconds. In Fig. 57 the theoretical curve is also shown, which is calculated on the basis of the dynamical theory of x-ray diffraction. The effect of convolution in the case of the double-crystal arrangement is taken into consideration.[74] The half-width value of the theoretical curve is 11.6″. It can be said that the thermo-cyclically annealed specimens of Fe-3 wt/% Si are almost ideally perfect.

5. 3. 3. Si[72]

Fig. 58 shows typical x-ray topographs of Si specimen before the thermal cyclic annealing taken on the same area under different diffracting vectors g. Here, the squared areas (denoted by N 1, N 2, and N 3) are those areas where Si_3N_4 film was deposited, while the remainder (denoted by M) was masked during deposition of Si_3N_4. Many dislocations were generated not only in N areas but also in M area during heating at 1373 K after the deposition of Si_3N_4. The results of contrast experiments are summarized in Fig. 59. The following can be seen;

1) All the dislocations observed are straight and parallel to one of <110> directions.

2) Pure edge, pure screw and 60 dislocations are observed; The Burgers vectors of these dislocations are <110>.

3) The pure edge dislocations are identified as Lomer dislocations. They are observed only in N area, while the pure screws only in M areas. The 60° dislocations exist in both M and N areas.

4) It is considered that the Lomer dislocations are formed as a result of the reaction between two glide dislocations gliding on non-parallel slip planes along the intersection of the two {110} slip planes. In the particular case shown in figs. 58 and 59 the reactions may be written as follows

$$\mathrm{BC}/\delta(\mathrm{E})+\mathrm{DB}/\gamma(\mathrm{G})=\mathrm{DC}(\mathrm{A}) \tag{1}$$

$$\mathrm{DA}/\beta(\mathrm{C})+\mathrm{BD}/\alpha(\mathrm{F})=\mathrm{BA}(\mathrm{B}) \tag{2}$$

where figures in parentheses stand for the types of dislocations summarized in Fig. 59.

Fig. 60 shows the x-ray topographs of the same area shown in Fig. 58 but after thermal cyclic annealings for 24 hours (b) and 100 hours (c). It is evident that density of the dislocations in both M and N areas decreased substantially as a result of the annealing. In particular, screw dislocations in M area (denoted by I and J in Fig. 59) disappeared almost completely. The dislocation density in N areas is also reduced greatly but the density of dislocations that survived the annealing is much larger in N than in M. Occassionally new dislocations such as one indicated by arrow A in Fig. 60 are formed during the annealing. Contrast experiment shows that these new dislocations are Lomer dislocations; presumably, these dislocations were formed by the reactions of eq. 2 during thermal cyclic annealing.

The variation of the density of total dislocations in Si during thermal cyclic annealing is plotted against the annealing time in Fig. 61 (a), together with the results for Cu,[68,69] Ag,[70] and Ag alloys.[70] The total density of dislocations in Si decreased with increasing annealing time in a manner similar to those for fcc metals and alloys. Furthermore, the densities of the Lomer, the 60° and the screw

dislocations in Si during thermal cyclic annealing are plotted against the annealing time in Fig. 61 (b). The following features can be seen in Fig. 61 (b). The pure screw dislocations disappeared very rapidly and the density was almost naught after an annealing for 24 hrs. The density of 60° dislocation decreased rapidly in the early stage of annealing and then more slowly in the later stage. In contrast to these two types of dislocation, the density of Lomer dislocations remained practically unchanged during an annealing of 100 hrs.

5. 4. Discussion and Conclusions

The reduction of dislocation density during a thermal cyclic annealing results from the mutual annihilation of dislocations.[68)69)] In order for the mutual annihilation to take place inside a crystal dislocations with same Burgers vectors but of oppoiste signs must meet each other. Except for pure screws, which can change the slip plane by cross slip, this process requires both glide and climb motion of dislocation, since it is unlikely that the dislocations of opposite signs lie on the same glide plane. The glide motion of dislocation is controlled by the frictional force acting on the dislocations, and the climb motion by the interaction with vacancies. At such a high temperature as just below the melting point the frictional force acting on the glide dislocations is expected to be very small even in Fe-Si and Si where the Peierls force is very high. Thermal cyclic annealing increases the opportunity of dislocations interacting with vacancies, thus enhancing the climb motion of dislocations. Thus, the mutual annihilation of glide dislocations is expected to take place very frequently during the thermal cyclic annealing even in Fe-Si and Si. Since screw dislocations need not climb for the mutual annihilation to take place, they will disappear much more rapidly than non-screw dislocations that must climb for the mutual annihilation to take place.

The situation for Lomer dislocations is quite different. The density of Lomer dislocations decreased only very slightly during the annealing. This can be rationalized as follows. Lower dislocations are sessile and very stable up to very high temperatures. In addition, the climb motion of the Lomer dislocations is also very difficult, since they are dissociated onto two non-parallel {111} planes to form Lomer-Cottrell dislocations. This is the reason why the density of Lomer dislocations did not decrease substantially during the thermal cyclic annealing.

From the above discussion it can be concluded that in those crystals where Lomer-Cottrell dislocations are likely to occur the effectiveness of the thermal cyclic annealing in reducing the dislocation density is limited to a great extent by the presence of the grown-in Lomer-Cottrell dislocations. Conversely, in those crystals where stable sessile dislocations such as Lomer-Cottrell dislocations are not formed (bcc, hcp) the thermal cyclic annealing is to be very effective in reducing the dislocation density.

6. Summary and Conclusions

For the purpose of observing melting and growth processes of metallic single crystals with relatively high melting temperature continuously, a Lang type topography camera with a high temperature furnace for unidirectional solidification

was constructed on a large goniometer of an ultra-high intensity x-ray generator (90 kW class) and a TV-VTR imaging system has been developed.

With the aid of these facilities, real time observations of melting and growth processes of aluminum and gallium single crystals and dendritic growth of Al-Mg alloys have been carried out.

In the first place, microscopical structure of the solid-liquid interface and the mechanism of growth from the melt are clarified.

In the case of aluminum whose Jackson's parameter α is about 1.3, it is found that:

(1) The solid-liquid interface during a crystal growth is rough.

(2) The growth is by the continuous growth (adhesive growth).

(3) When a crystal grows at a rate faster than a certain value (about 40 μm/s in the present experiments) or when the growth rate is changed to exceed such value, many dislocations are generated into the newly grown region of the aluminum crystal.

In the case of gallium whose α parameter ranges 1.12~2.24 depending on the growth direction, it is found that;

(1) The solid-liquid interface is smooth.

(2) The growth is by the lateral growth, and the rate of lateral spread of nuclei is almost the same as that of nucleation.

(3) New findings which cannot be predicted by the Jackson's theory were obtained on the growth process of gallium, so that this theory has to be modified, although the theory seems to be of general validity. One of the modifications proposed is to take into account the second nearest neighbour atoms in calculating the α parameter.

In the case of the dendriric growth of Al-Mg binary alloys, it is found that

(1) The primary dendrite arms grow always in $\langle 100 \rangle$ direction at the growth rate studied in the present experiments (10 μm/s~90 μm/s) even if macroscopic growth direction is varied.

(2) Angle extended between the primary arms and the secondary arms of the dendrite depends on the growth rate and the Mg content.

(3) There is a considerable difference in the concentration of Mg between the primary arms and other high-order arms.

Morphological as well as microstructural changes of aluminum single crystals and dendrite arms of Al-Mg alloys were observed during cooling and isothermal annealing after solidification. Generation and multiplication of dislocations arise from decreasing the temperature at a rate faster than a certain rate. The formation of dislocation bundles or subgrain boundaries are due to annealing at the temperature near the melting point just after the solidfication, so that the cooling rate has to be very low in order to suppress dislocation nucleation. In addition, it is found that morphology of dendrite arms changes just after the solidification. Lattice distorsion of dendrite arms takes place and morphological change as well as microstructural change of dendrite arms followed over the whole crystal. These changes are likely caused by the stress due to shrinkage of crystal or segregation of Mg atoms. The microstructural change of dendrite arms during isothermal annealing near the melting point is attributable to the solute redistribution caused by diffusion in solid.

As regards the origin of dislocations, careful observations of the advancing crystal front near the solid-liquid interface and cooling process of the newly grown

crystal were made. In the case of aluminum, a dislocation-free region was observed in adjacent to the advancing front. It was also observed that many dislocations were generated behind this dislocation-free region when the cooling speed was high. In the case of gallium single crystal from a highly perfect seed, no dislocations were generated over the whole area of a crystal. From the observations made in the present studies, it is concluded that the origin of dislocations associated with solidification is vacancy condensation.

Finally, it seems worth mentioning that thermal cyclic annealing introduced in the present experiments is very useful to reduce the density of dislocations in single crystals of fcc, bcc and diamond structures.

7. Refereces

1) J. Chikawa: J. Cryst. Growth **24/25** (1974) 61.
2) J. Chikawa and S. Shirai: J. Cryst. Growth **39** (1977) 328.
3) J. Chikawa and F. Sato: "Defects and Radiation Effects in Semiconductors. 1980" ed. R. R. Hashiguti (The Institute of Physics. 1981) p. 95.
4) J. Chikawa and F. Sato: "Defects in Semiconductors" eds. Narayan and Jan. (North-Holland. 1981) p. 317.
5) K. A. Jackson, D. R. Vhlmann and J. D. Hunt: J. Cryst. Growth **1** (1967) 1.
6) D. E. Glicksman and P. W. Voophees: Metallur. Trans. **15A** (1984) 995.
7) I. Gutzow and E. Parcheva: Krystall und Technik **11** (1976) 793.
8) M. E. Glicksman R. J. Schaefer: J. Cryst. Growth **1** (1967) 297.
9) K. A. Jackson and J. D. Hunt: Acta Met. **13** (1965) 1212.
10) K. A. Jackson, J. D. Hunt, D. R. Vhlman and T. P. Seward III: Trans AIME **236** (1966) 149.
11) M. E. Glicksman and P. W. Voophees: Metallur Trans. **15A** (1984) 995.
12) J. D. Hunt and K. A. Jackson: Trans AIME **236** (1966) 843.
13) J. D. Hunt and K. A. Jackson: Trans AIME **239** (1967) 864.
14) D. G. McCartney and J. D. Hunt: Acta Met. **29** (1981) 1851.
15) G. A. Chadwick: Acta Met. **10** (1962) 1.
16) T. Okamoto and K. Kishitake: J. Cryst. Growth **29** (1975) 137.
17) T. Kobayashi and T. Imura, Japn. J. Appl. Phys. **23** (1984) L632.
18) T. Kobayashi, T, Imura and Y. Nishikawa, Japn. J. Appl. Phys. **25** (1986) 345.
19) O. Nittono, T. Ogawa, S. K. Gong and S. Nagakura: Jpn. J. Appl. Phys. **23** (1984) L531.
20) H. E. Cline: Trans AIME **239** (1967) 1489.
21) C. Lemaigman, D. Camel and J. Pelissier: J. Cryst. Growth **52** (1981) 67.
22) R. Hamer and C. Lemaigman: J. Cryst. Growth **53** (1981) 586.
23) H. Saka, A. Sakai, T. Kamino, and T. Imura: Phil. Mag. (a) **52** (1985) L29.
24) M. E. Glicksman: "Solidification", T. J. Hughel and G. F. Bolling eds. (American Society for Metals, Metal Park 1970) pp. 155.
25) K. A. Jackson: "Liquid Metals and Solidification" (American Society for Metals, Cleveland, 1958) 174.
26) K. A. Jackson, and D. Chalmer: Can. J. Phys. **34** (1956) 473.
27) K. A. Jackson, D. R. Vhlman and J. D. Hunt: J. Cryst. Growth **1** (1967) 1.
28) Y. Nishino, M. Suzuki, T. Tono, H. Saka and T. Imura: Jpn. J. Appl. Phys. **20** (1981) 1553.
29) Y. Nishino, H. Saka and T. Imura: Phys. Status Solidi (a) **70** (1981) 729.
30) Y. Nishino and T. Imura: Jpn. J. Appl. Phys. **21** (1982) 1283.
31) J. Chikawa: J. Cryst. Growth **24/25** (1974) 61.

32) T. Imura and Y. Nishino, X-Ray Instrumentation for Photon Factory "Dynamic Analyses of Micro Structure in Matter" ed. by S. Hosoya et al. KTK Scientific Pub., Tokyo (1986) 337-348.
33) F. Weinberg and B. Chalmers: Can. J. Phys. **30** (1952) 488.
34) F. Weinberg and B. Chalmers: Can. J. Phys. **29** (1951) 382.
35) J. W. Cahn: Acta Met. 8 (1960) 554.
36) G. Harvay and J. W. Cahn: Acta Met. **9** (1961) 695.
37) G. A. Chadwick: Acta Met. **10** (1962) 1.
38) R. Rosenberg and W. C. Winegard: Acta Met. **2** (1954) 342.
39) G. Horvay and J. W. Cahn: Acta Met. **9** (1961) 695.
40) G. F. Bolling and J. W. Cahn: J. Appl. Phys. **32** (1961) 2587.
41) P. E. Brown and M. Adams, Jr.: Trans. Am. Foundrymen's Soc. **69** (1961) 879.
42) H. D. Brody and N. C. Flemings: Trans. Met. Soc. AIME **236** (1966) 615.
43) D. E. Temkin: Soviet Phys. Doklad.: **5** (1960) 609, Crystallization Process (Consnltant Bureau, N. Y. 1966) 15.
44) W. Kurz and D. J. Fisher: Acta Met. **29** (1981) 11.
45) D. G. McArtney and J. D. Hunt: Acta Met. **29** (1981) 1851.
46) C. M. Claren, J. D. Verhoseven and R. Trivedi: Metallur. Trans. **11A** (1980) 1853.
47) T. Okamoto and K. Kishitake: J. Cryst. Growth **29** (1975) 133.
48) S. N. Tewari and A. M. Srioammurthy: Metallur. Trans. **12A** (1981) 137.
49) K. P. Toung and D. H. Kirwood: Metallur. Trans **6a** (1975) 197.
50) W. Morris, W. A. Tiller, J. W. Rutter and W. C. Winegard: Trans ASM **47** (1954) 463.
51) E. L. Holmes, J. W. Rutter and W. C. Winegard: Can, J. Phys. **35** (1957) 1223.
52) H. E. Cline: Trans AIME **239** (1967) 1489.
53) C. Lemaignan, D. Camel and J. Pelisier: J. Cryst. Growth **52** (1981) 67.
54) R. Hamar and C. Lemaignan: J. Cryst. Growth **53** (1981) 586.
55) T. Kobayashi, Y. Nishikawa and T. Imura: Jpn. J. Appl. Phys. **25** (1986) 345.
56) A. Watanabe, A. Sudo, U. Honma and S. Oya: Aluminum: **58** (1982) 346.
57) W. Kurz and D. J. Fisher: Acta Met., **29** (1981) 11.
58) K. E. Glicksman and P. W. Voorhees: Metallur. Trans. **15A** (1984) 995.
59) S. Mizushima: J. Phys, Soc. Japan **12** (1960) 70.
60) A Ookawa: J. Phys, Soc. Japan **12** (1960) 2191.
61) D. Kuhlmann-Wilsdorf: Phys, Rev. **10A** (1965) 1599.
62) I. A. Kotze and D. Kuhlmann-Wilsdorf: Phil. Mag, **23** (1971) 1133.
63) R. M. Cotterill, E. J. Jensen, W. W. Damgaad Kristeusen and R. Paetsch: J. de physique **36** (1975) C2-35.
64) H. Suzuki: Bull. J. Inst. Met. **13** (1974) 733.
65) K. Kamada: Prog. Crystal Growth Charact, **3** (1981) 309.
66) G. Shoeck and W. A. Tiller: Phil. Mag. **5** (1960) 43.
67) G. F. Bolling and D. Fainstein: Phil Mag. **25** (1972) 45.
68) S. Kitajima, M. Ohta and H. Kaieda: J. Japan. Inst. Metals, **32** (1968) 164.
69) S. Kitajima, M. Ohta and H. Tonda: J. Crystal Growth **24/25** (1974) 521.
70) H. Suga and T. Imura: Trans. Japan. Inst. Metals **17** (1976) 605.
71) H. Saka, A. Sakai, T. Imura, S. Nakatani and S. Kikuta: Phys. Stat. Solid (a) **101** (1987) 51.
72) A. Sakai, H. Saka and T. Imura: Phys. Stat. Solidi (a) **97** (1986) 57.
73) R. H. Hammer, W. C. T. Yech, T. G. Oakwood and A. A. Henderickson: Trans. AIME **239** (1967) 1962.
74) R. W. James: The Optical Principles of Diffraction of X-Rays, G. Bell & Sons, London 1962.

8. Acknowledgement

The authors would like to express their sincere thanks to the members of the metal physics laboratory, in particular, Dr. K. Kuroda, Mr. Y. Nishikawa and Mr. N. Okamoto for their cooperation in carrying out the present experiments. Thanks are also due to Mr. K. Yasuda for his assistance in operating the ultra high intensity x-ray unit of Nagoya University.

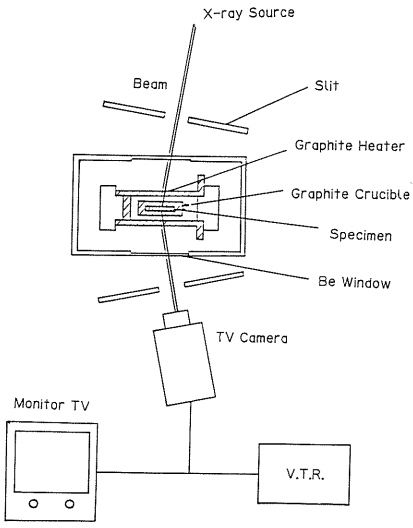

Fig. 1. Schematic diagram of x-ray topography system consisting of a Lang type camera with a TV-VTR imaging system and a specimen-heating facility.

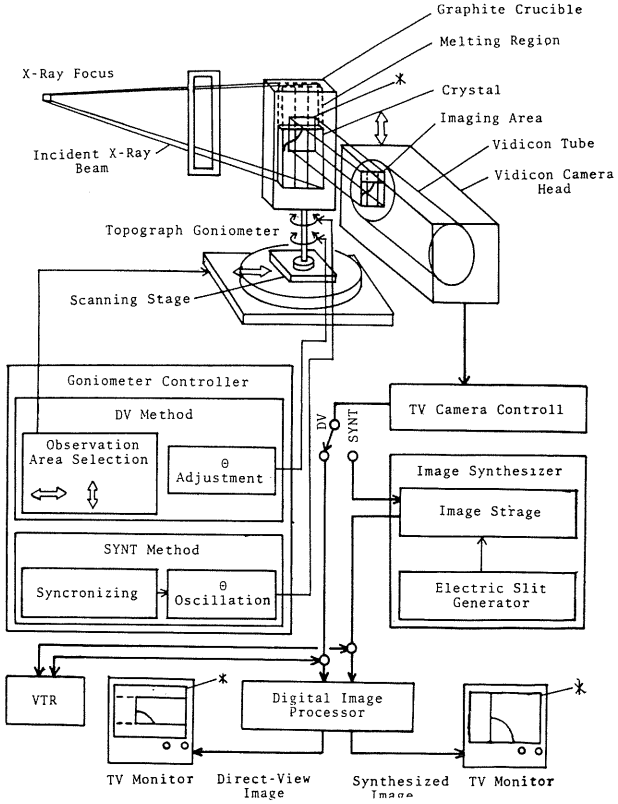

Fig. 2. Block diagram of the TV-VTR imaging system used for x-ray topography.

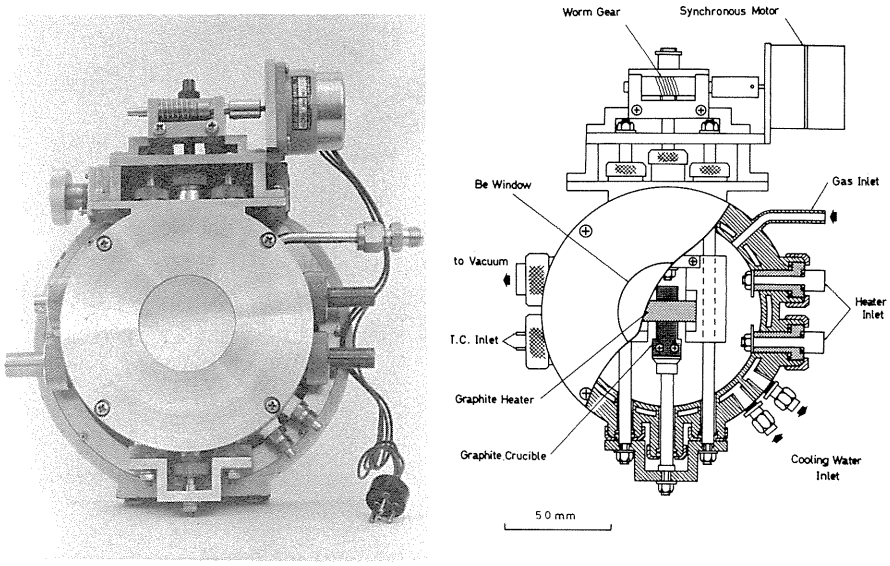

Fig. 3. Overview of the furnace for in-situ observations of the melting and growth processes with x-ray topography (a) and schematic illustration of it (b).

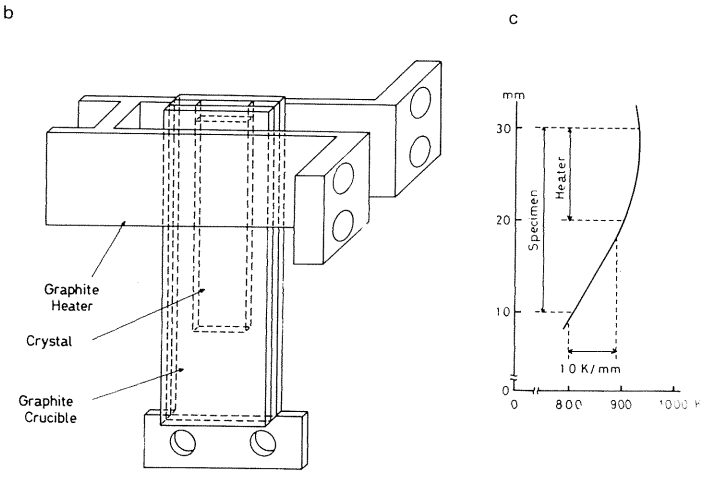

Fig. 4. Schematic illustration of graphite heater and graphite crucible (a) and the temperature gradient in the crucible (b).

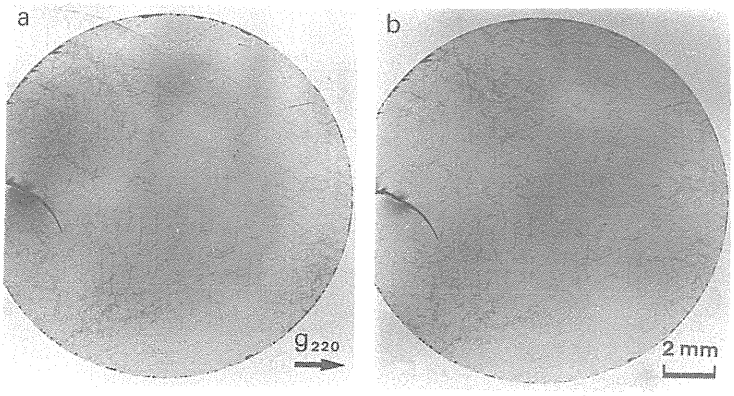

Fig. 5. X-ray topographs of Si crystal without interposing graphite plates (a) and with interposing graphite plates (b).

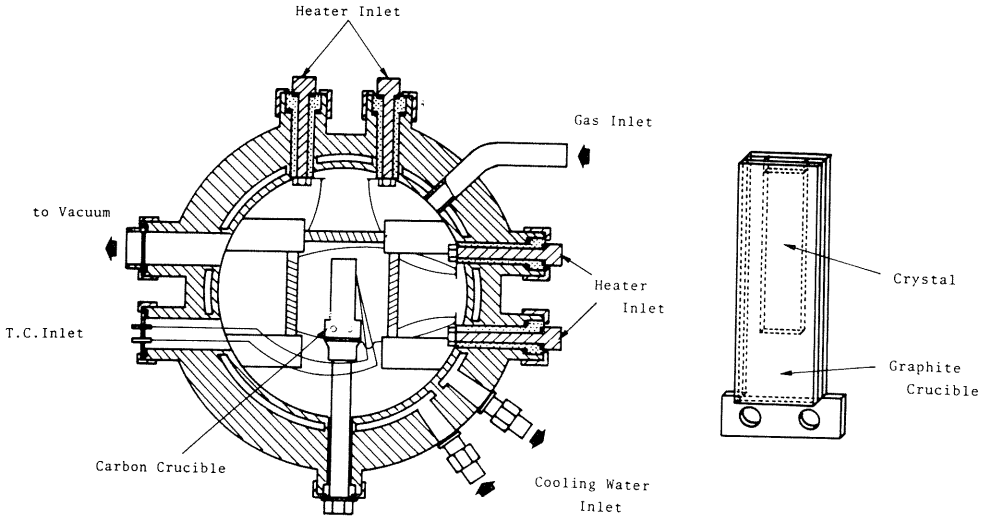

Fig. 6. Schematic drawings of a Bridgman furnace (a) and the graphite crucible (b) for in-situ observations of melting and growth by x-ray topography.

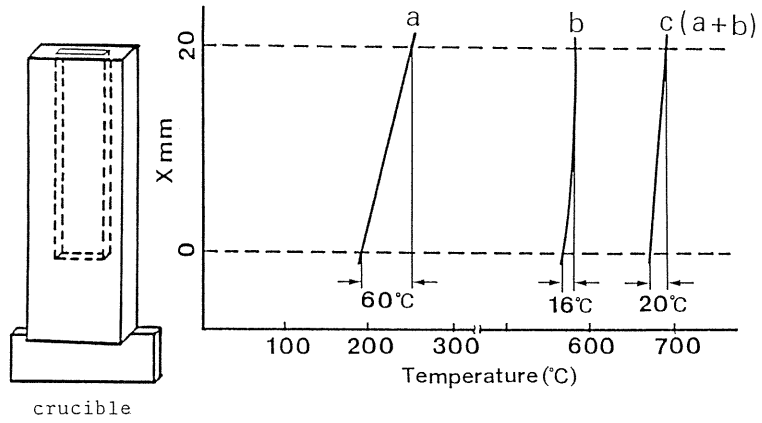

Fig. 7. Temperature gradients of the specimen in the crucible heated with the upper heater (a), with the side heaters (b) and with the upper and the side pairs operated (c).

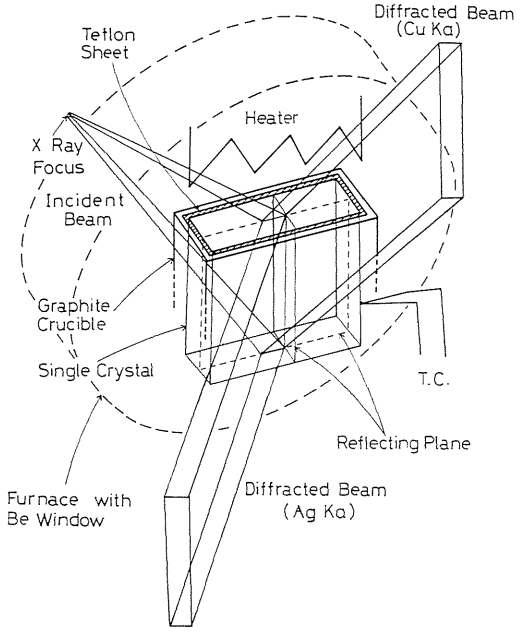

Fig. 8. Schematic drawing of the disposition of x-ray source, graphite crucible, heater and diffracted beam for in-situ observations of melting and growth processes of gallium.

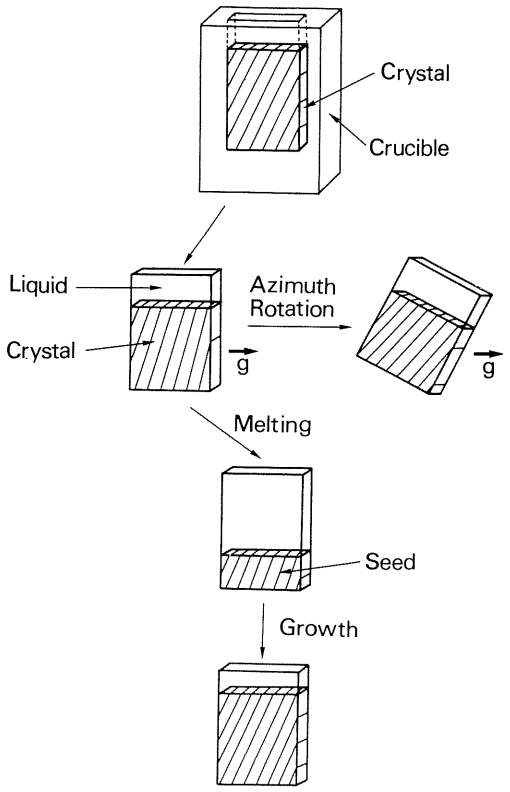

Fig. 9. Schematic representation of the specimen situation for observing melting and growth.

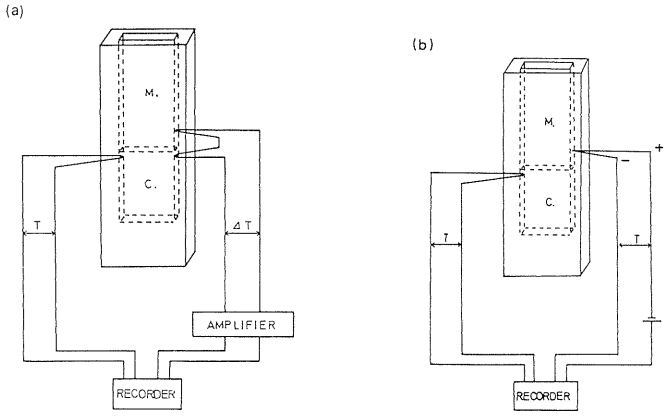

Fig. 10. Schematic diagram indicating the crucible and the thermo-couples used for the measurement of supercooling (a) and for the measurement of cooling rate (b).

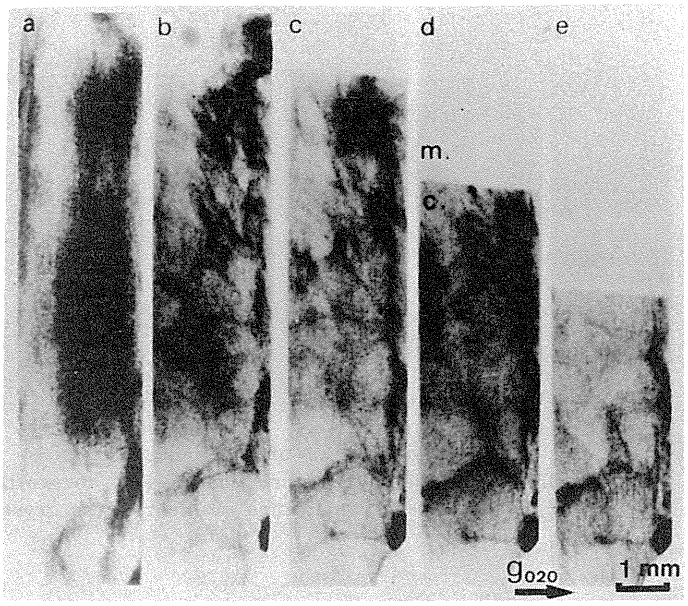

Fig. 11. A series of x-ray topographs (TV images) of aluminum single crystal (99.998%) prepared by strain-anneal method, the image at room temperature (a), the image just before the melting point (b) and the images observed during the melting process. Temperature gradient is 10K/mm near the melting point and the mean melting speed is about 12 μm/s.

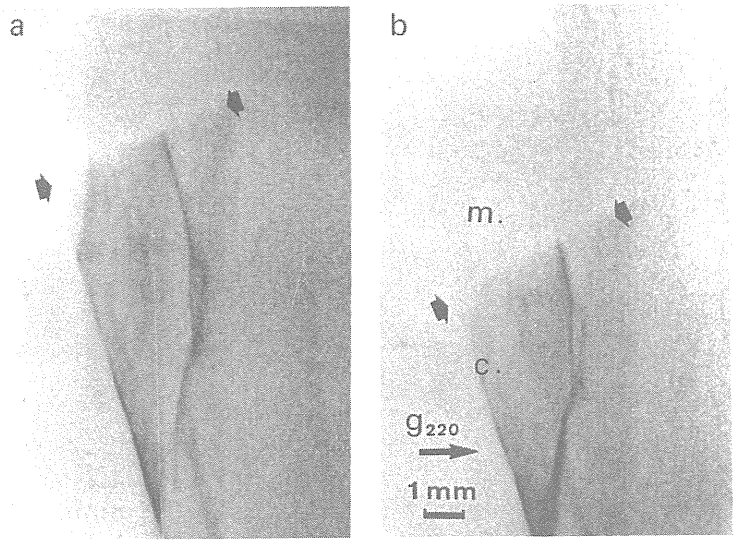

Fig. 12. X-ray topographs of an aluminum single crystal (99.998%) taken in the melting process, (a) to (b). The temperature gradient of the crystal: 1.0 K/mm.

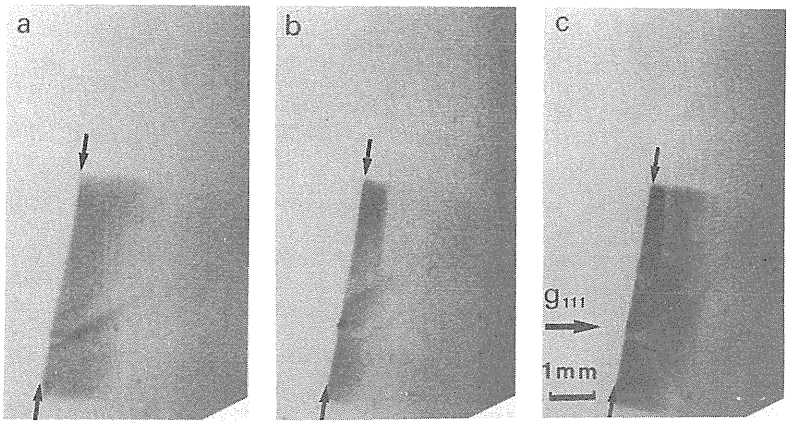

Fig. 13. A series of x-ray topographs of aluminum (99.998%) taken during horizontal melting along the direction normal to iso-thermal plane (indicated by arrows). Temperature gradient of the crystal: 1.0 K/mm.

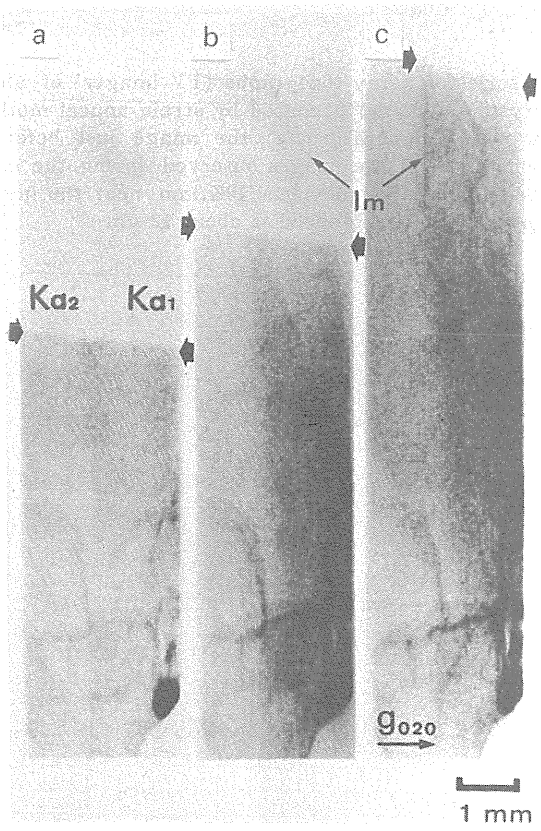

Fig. 14. A series of x-ray topographs of aluminum during the subsequent growth of the crystal shown in Fig. 11. Mean growth rate was about 20 μm/s in (a) to (c). Solid-liquid interface is indicated by bold arrows. The arrows with Im indicate the images of mica used for thermal shield.

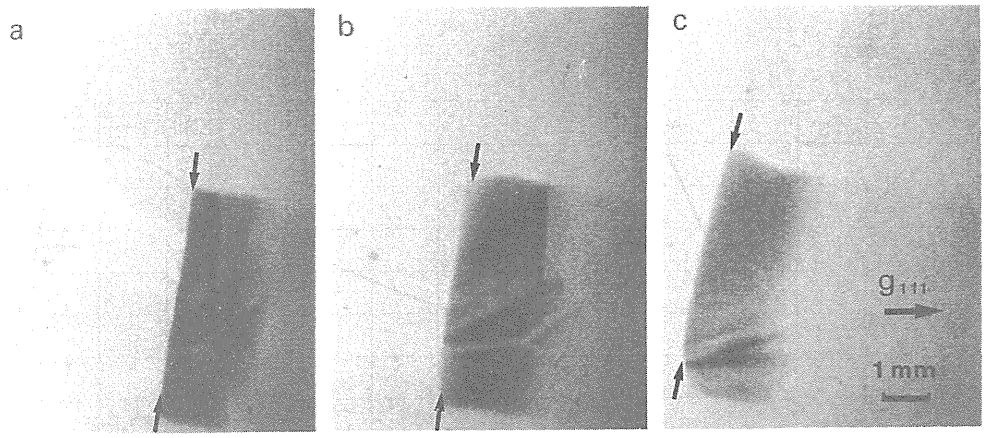

Fig. 15. A series of x-ray topographs of aluminum taken in the growth process subsequent to Fig. 13. The growth rate: 19 μm/s, temperature qradient: 1K/mm.

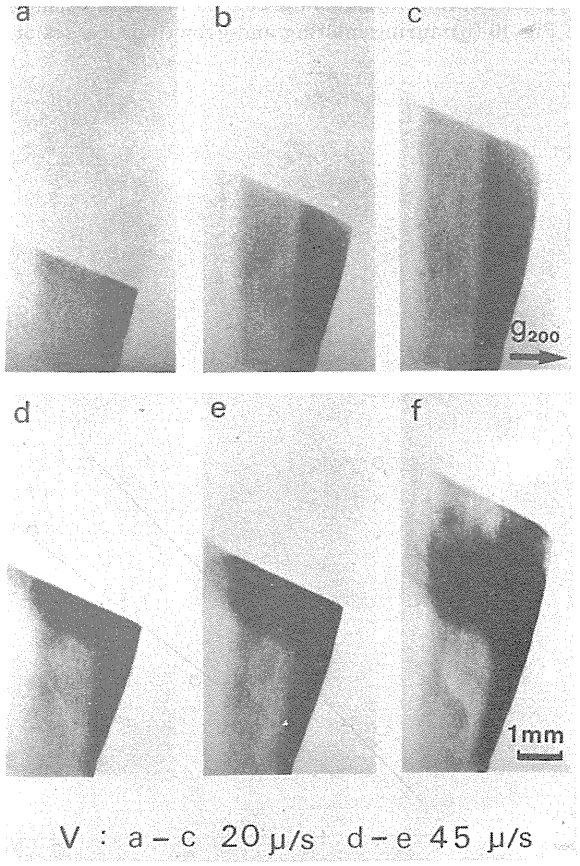

Fig. 16. A series of x-ray topographs of aluminum (99.999%) taken during growth process. The growth rate of (a) to (c) was about 20 μm/s and that of (d) to (f) was about 45 μm/s.

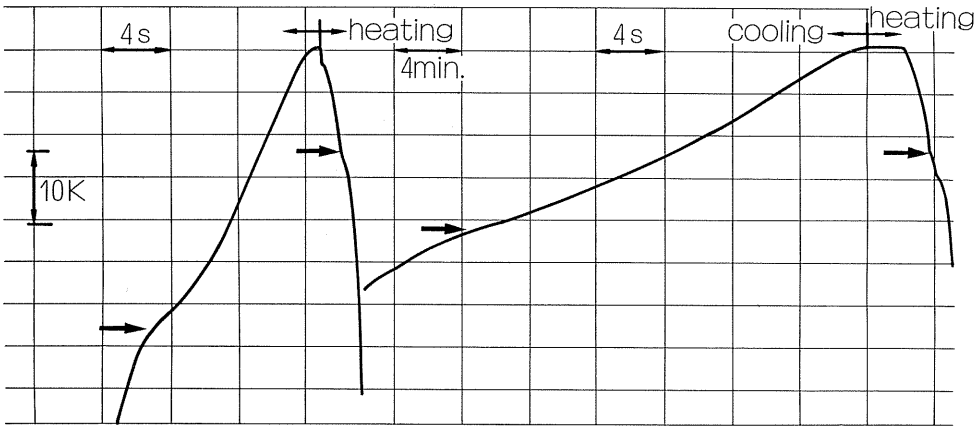

Fig. 17. Typical heating and cooling curves measured using the crucible shown in Fig. 10 (b) during melting and growth processes of aluminum (99.999%).

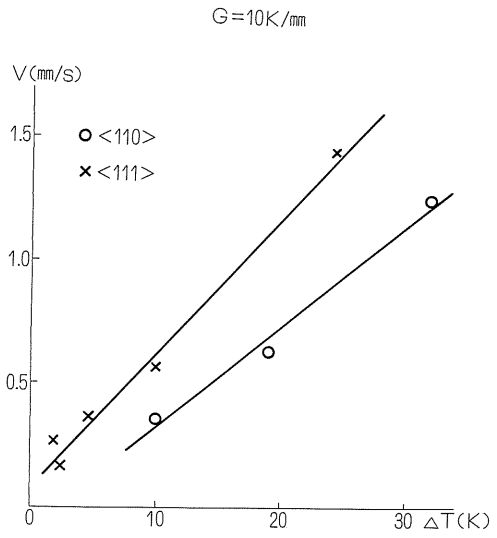

Fig. 18. Relations between growth rate and supercooling measured during the growth of aluminum in [110] and [111] directions.

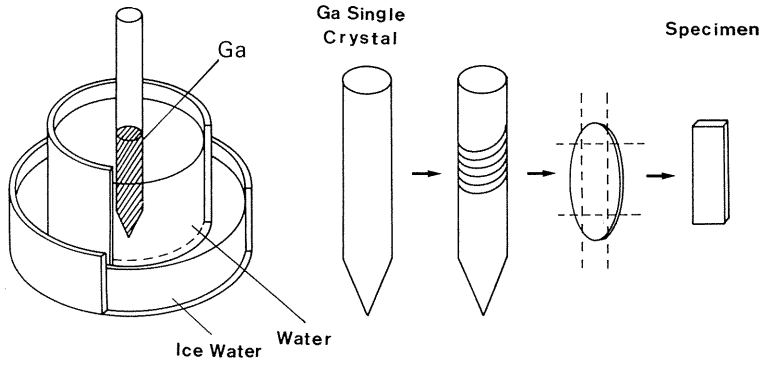

Fig. 19. Schematic illustrations of the procedure of preparing a gallium single crystal plate.

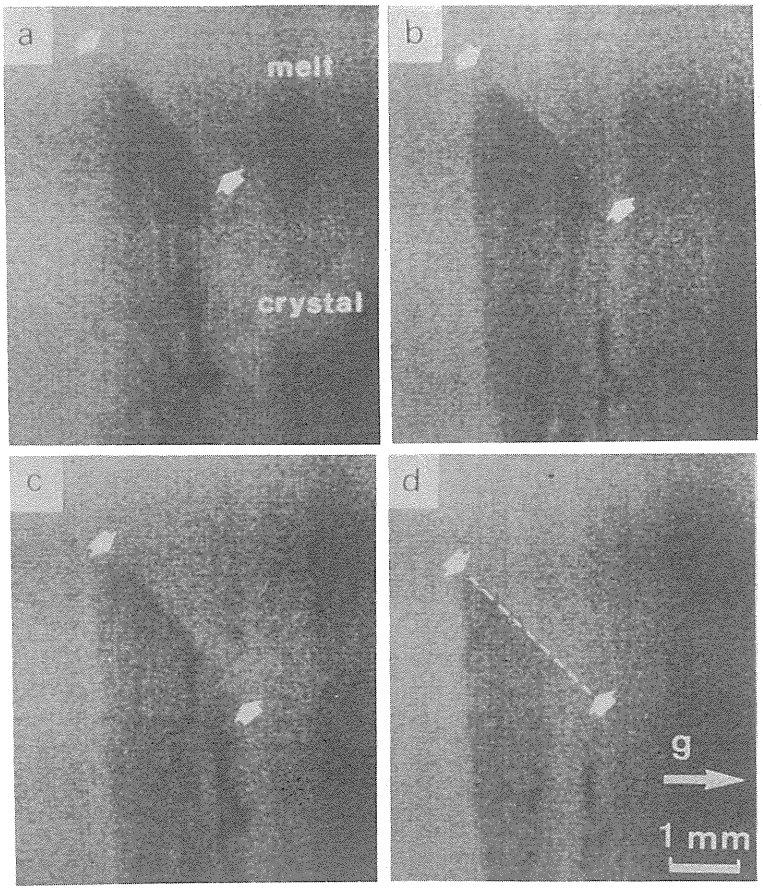

Fig. 20. A series of reflection topographs of TV images taken during the melting process of a gallium single crystal. Temperature gradient of the crystal: about 0.4 K/mm. The solid-liquid interface is indicated by arrows and a broken line.

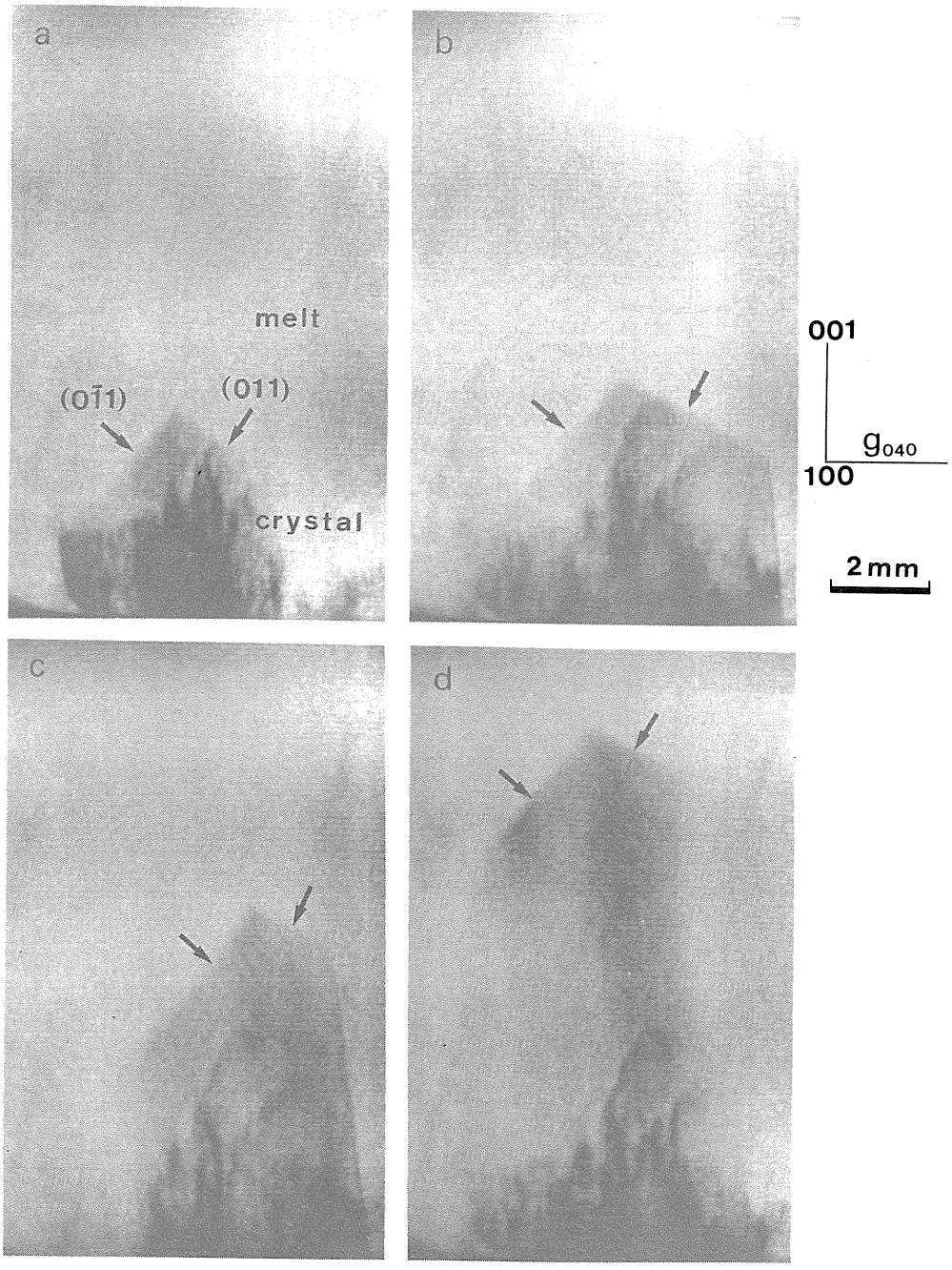

Fig. 21. A series of x-ray topographs taken during the growth of gallium. These images are TV images with an interval of about 100s. The faceted interfaces between the melt and the crystal lying along (0$\bar{1}$1) and (011) planes are indicated by arrows. The growth rates normal to each facet are as follows: (a)—(b) 0 μm/s. (b) to (c); 4 μm/s. (c), (c) to (d) 17 μm/s for (011) facet and (a)—(b) 5μm/s, (b)—(c) and (c)—(d) 12 μm/s for (011) facet.

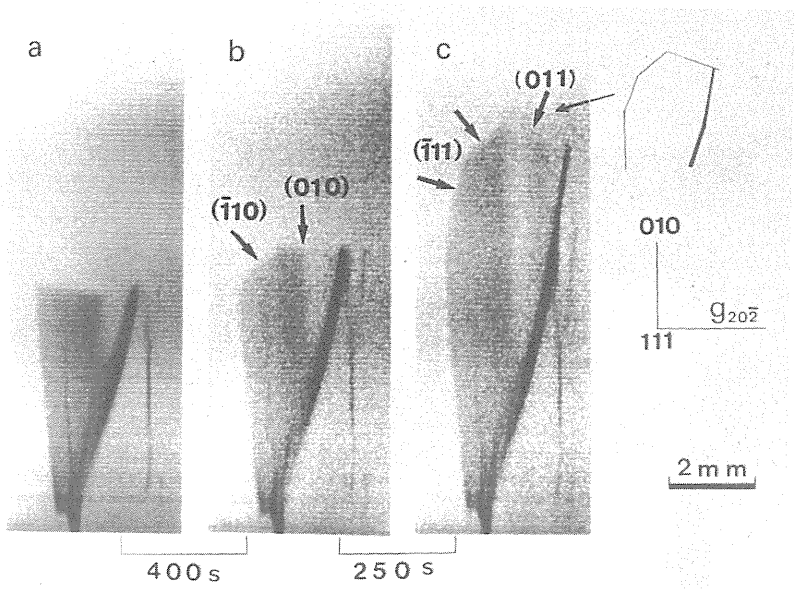

Fig. 22. A series of reflection topographs of equilibrium state (a), and growth process (b) and (c) in gallium. The figures indicated under the topographs are intervals. (1̄10) and (010) facets appear on (b) and (1̄11), (1̄10) and (011) facets on (c), and indicated by arrows. (d) is a schematic diagram of faceted interfaces of (c).

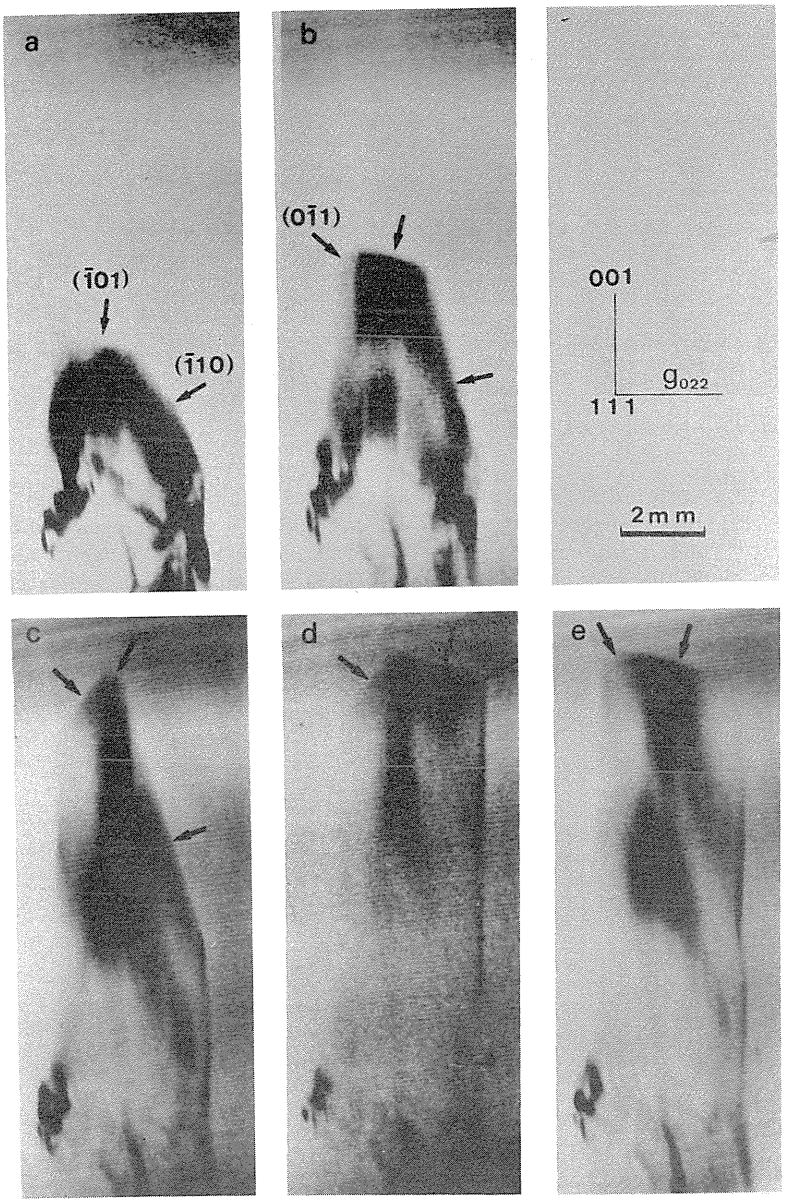

Fig. 23. Transmission topographs taken during growth of a gallium single crystal. (1̄01), (1̄10) and (01̄1) facets appear and compete with each facet. The growth rates normal to each facet are as follows; (a)—(b) 13 μm/s, (b)—(c) 12 μm/s and (d)—(e) 0 μm/s for (1̄01) facet, (b)—(c) 5 μm/s, (c)—(d) 0 μm/s, (d)—(e) 1 μm/s for (01̄1) facet, and (a)—(b) and (b)—(c) 2 μm/s, (c)—(d) 3 μm/s, (d)—(e) 0 μm/s for (1̄10) facet.

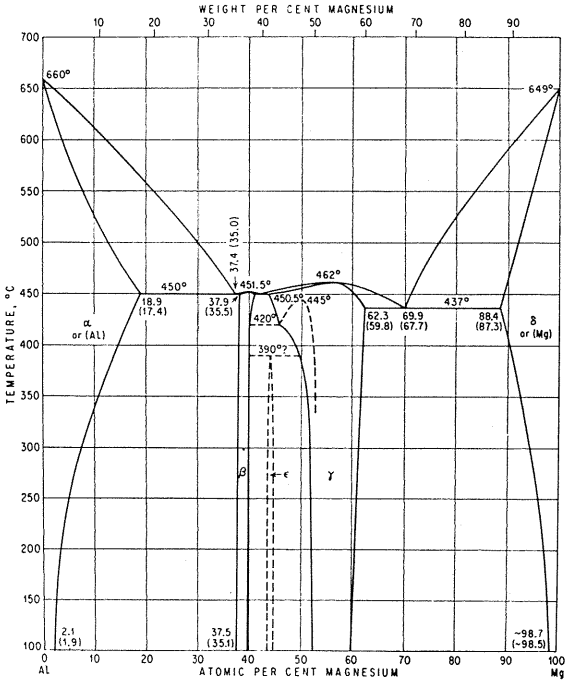

Fig. 24. Phase diagram of Al-Mg binary system. Specimens used in this study contain 0.5, 2.0 and 4.0 at. % Mg.

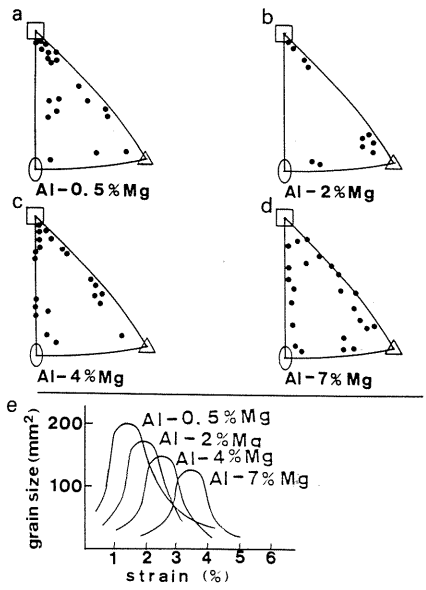

Fig. 25. Stereographic projection of the surface normals of recrystallized grains obtained by strain-anneal method of Al-Mg alloys of various Mg content, (a)—(d). The relationships between strain and grain size of the alloys are shown in (e).

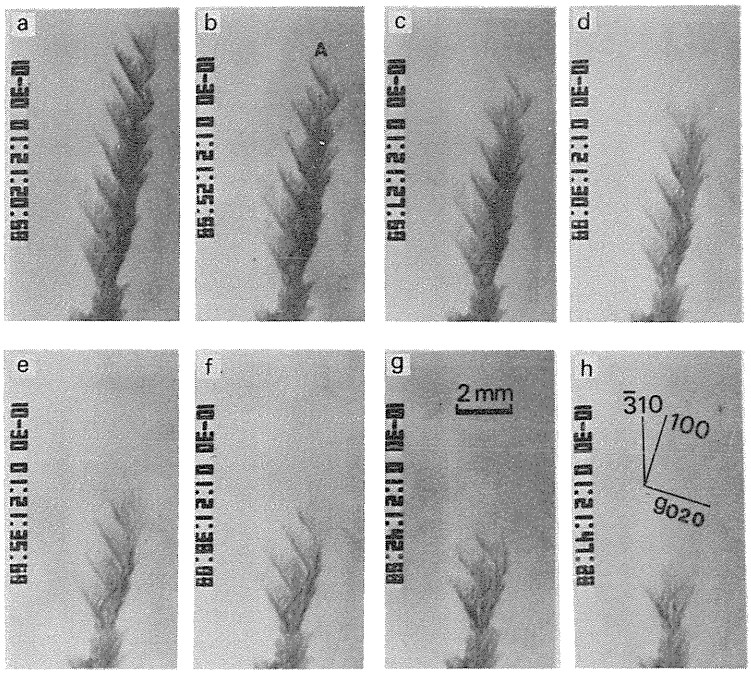

Fig. 26. A series of x-ray topographs of Al-4at.% Mg taken during the melting process.

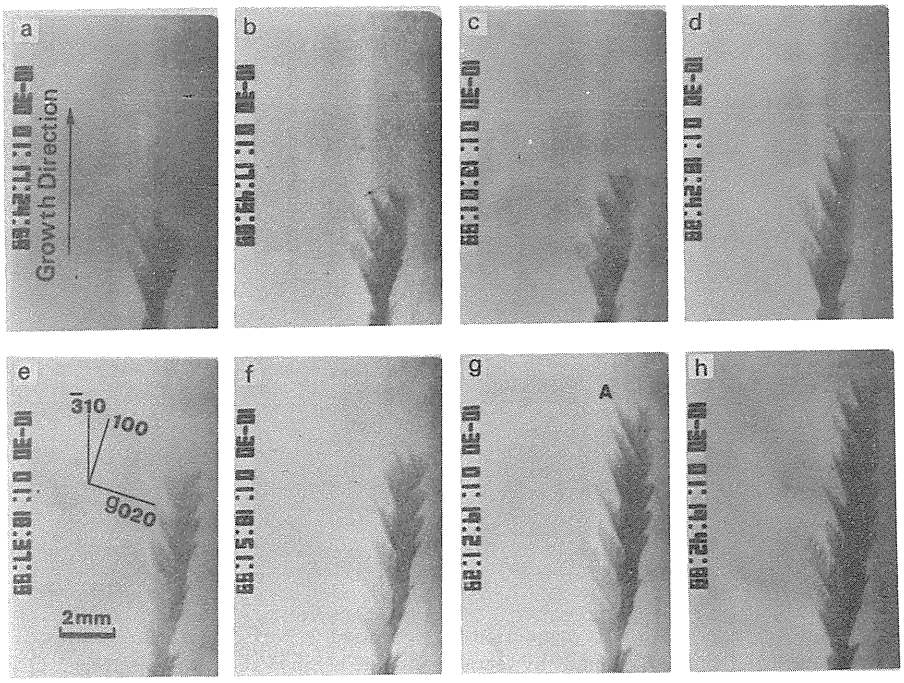

Fig. 27. A series of x-ray topographs of Al-4at.% Mg taken during the growth process.

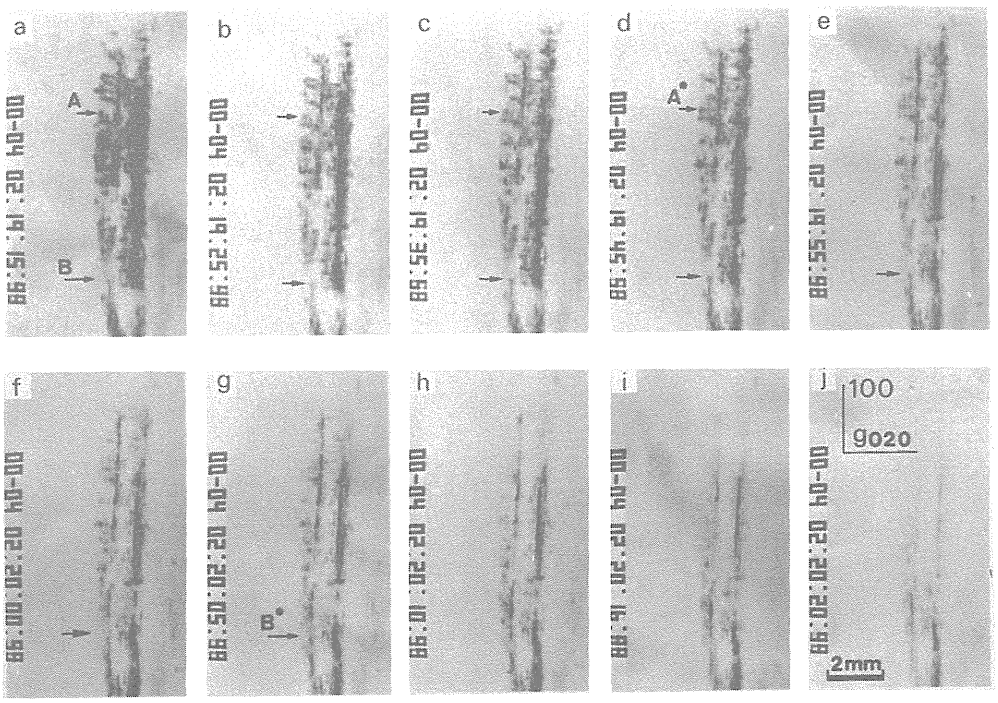

Fig. 28. A series of x-ray topographs of Al-4at.%Mg taken during the melting process.

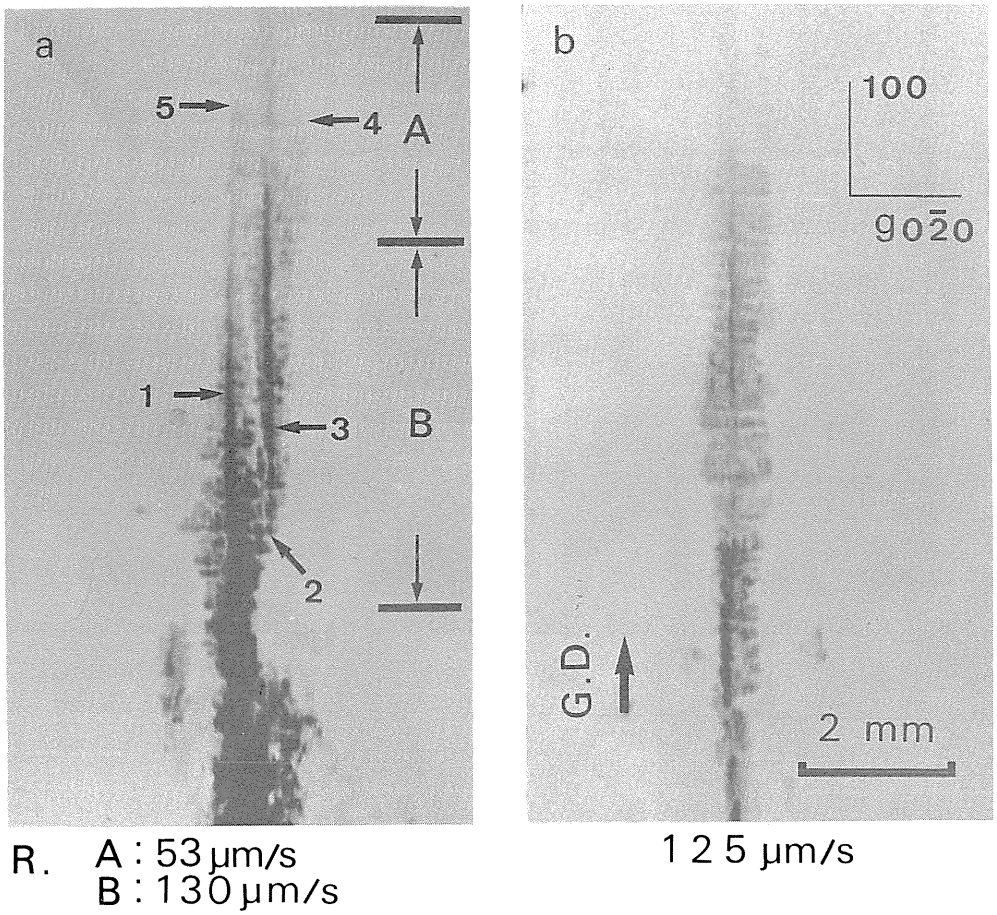

Fig. 29. X -ray topographs recorded on nuclear research plates showing morphological change of dendrite arms of Al-4.0at. % Mg as a function of the growth rate. Numbers at the bottom of the topographs refer to the growth rates. The growth direction and the reflection vector, g, are shown at the upper right corner of (b).

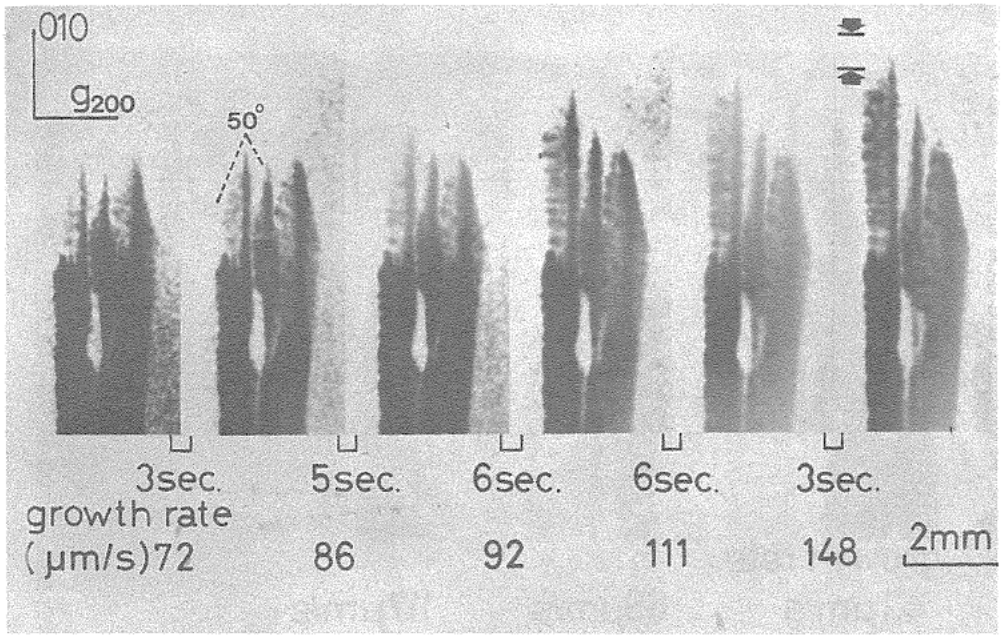

Fig. 30. A series of x-ray topographs of Al-4at.%Mg taken by changing the growth rate continuosuly.

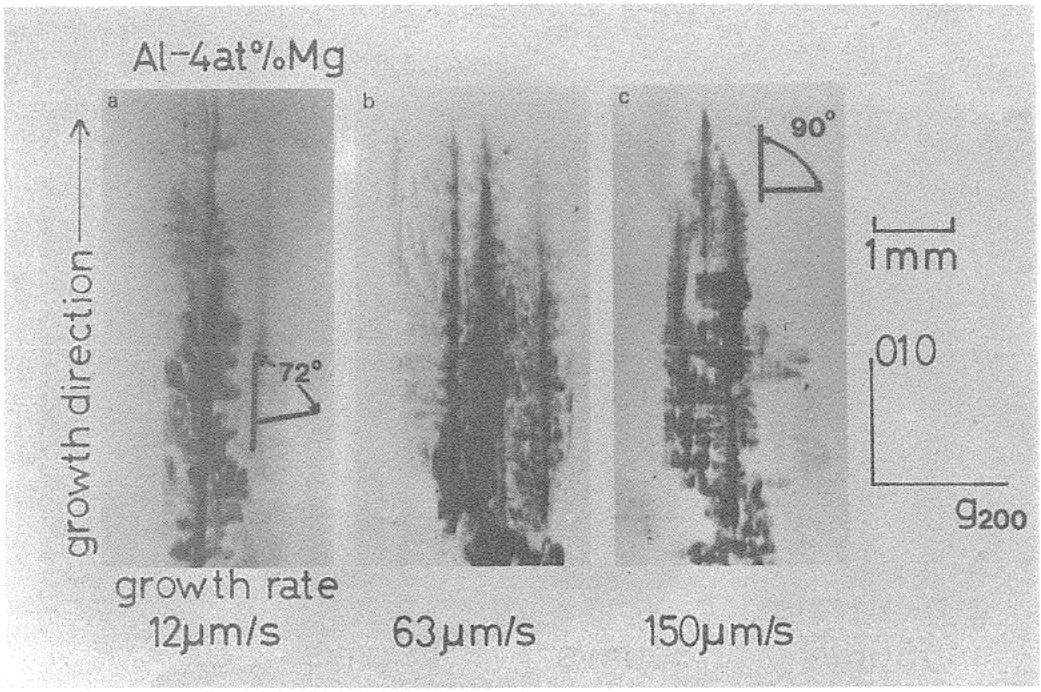

Fig. 31. X-ray topographs illustrating morphological change of Al-4 at.% Mg dendrites in changing the growth rate from 12 to 150 μm/sec.

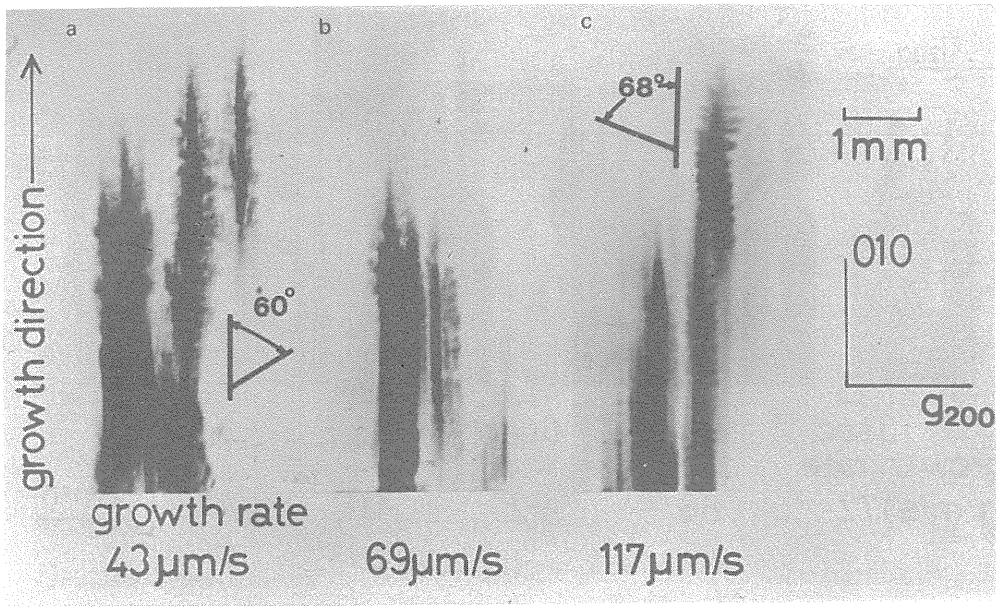

Fig. 32. X-ray topographs showing the effect of the growth rate on the angle between the primary and secondary arms of the dendrites in Al-2 at.% Mg.

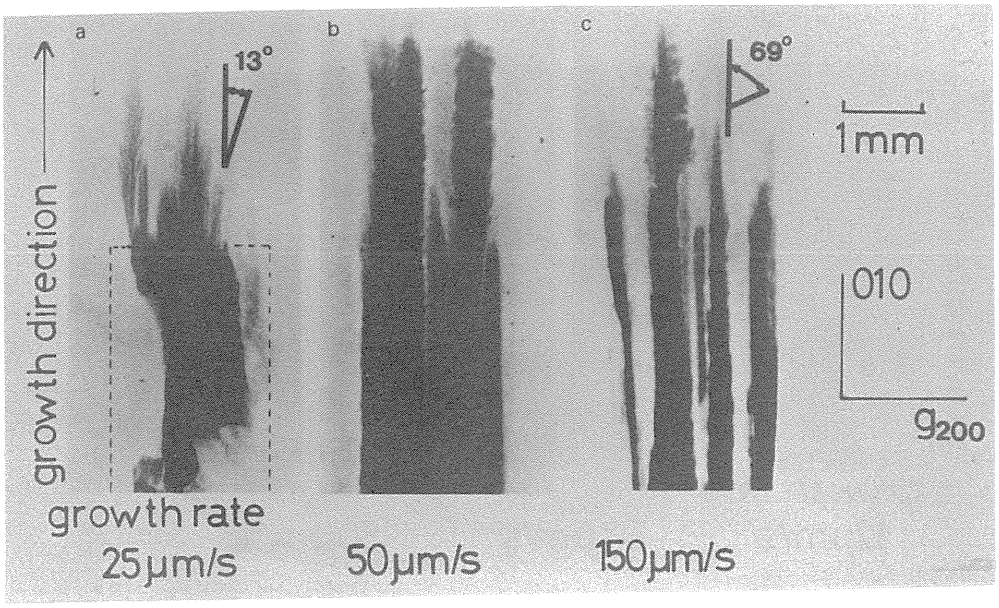

Fig. 33. X-ray topographs showing the effect of the growth rate on the angle between the primary and secondary arms of the dendrite in Al-0.5 at.% Mg.

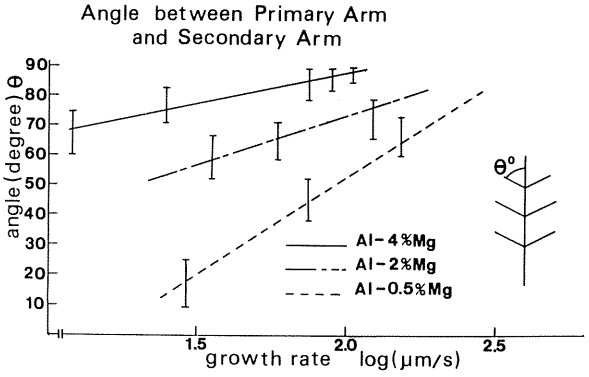

Fig. 34. Effect of the growth rate and Mg content on the angle θ between the primary and the secondary arms of the dendrite grown under the temperature gradient 1 K/mm.

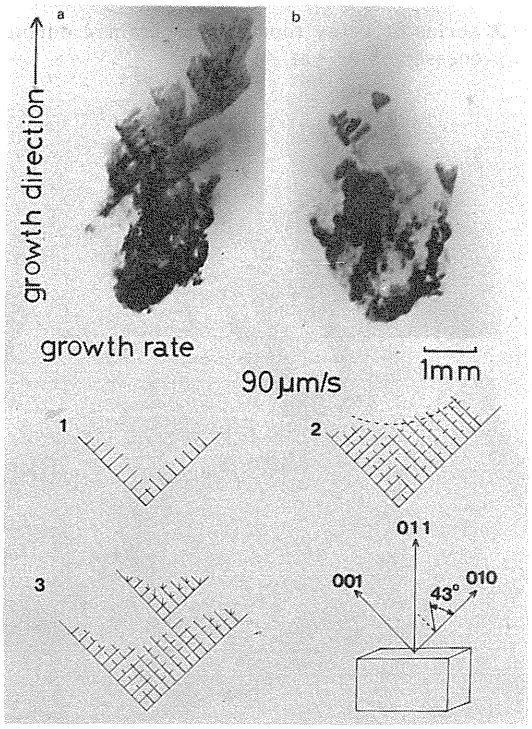

Fig. 35. Illustration of the change of dendrite morphology of an Al-4 at.% Mg recorded on nuclear research plate during the growth in ⟨110⟩ direction at a rate of 90 μm/s. The image of (b) was recorded by rotating the crystal by about 0.05° aroound the vertical axis relative to the position of (a). (020) reflection was used.

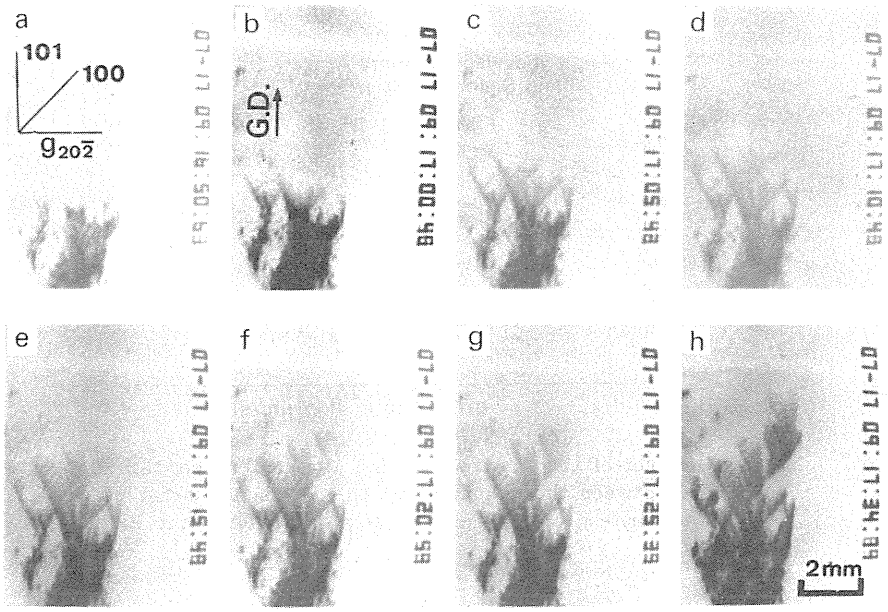

Fig. 36. A series of x-ray topographs obtained during the growing processes of Al-4 at. % Mg.

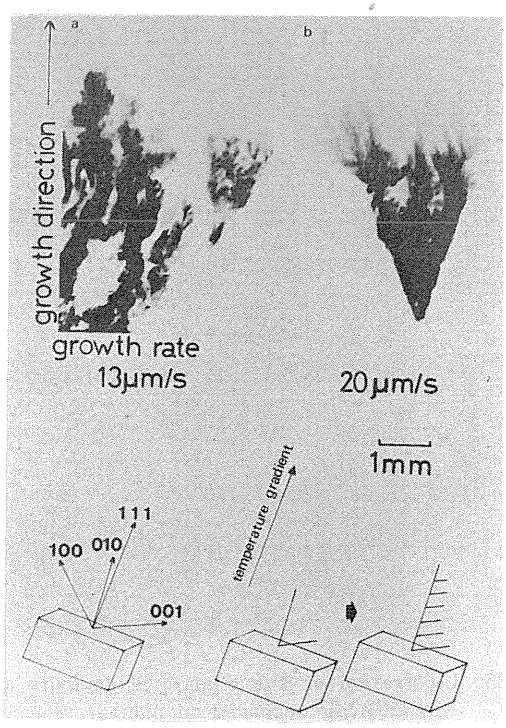

Fig. 37. Change of dendrite morphology of an Al-4 at.% Mg during ⟨111⟩ growth. These images were recorded on nuclear reseach plates with a short interruption of the growth. (002) reflection was used.

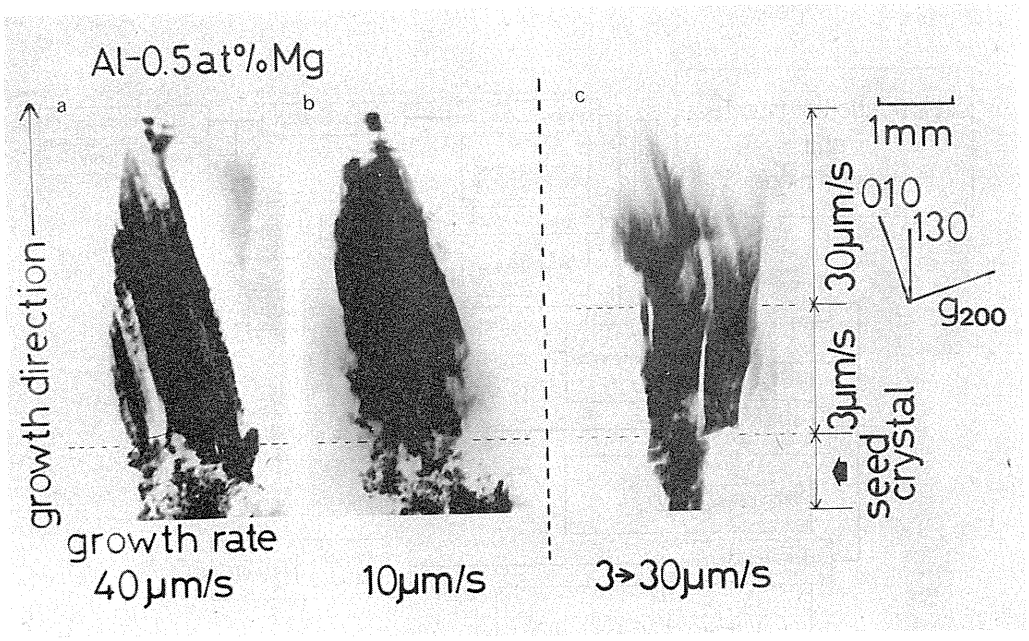

Fig. 38. Change of dendrite morphology of an Al-0.5 at.% Mg during ⟨130⟩ growth.

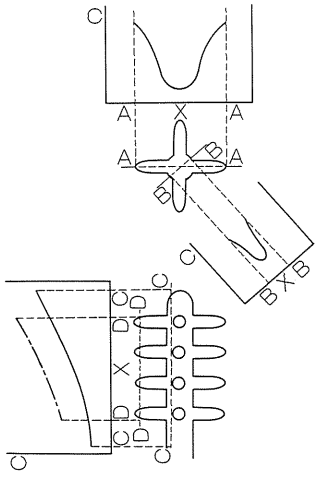

Fig. 39. Schematic illustration of the concentration profiles of Mg in a columnar dendrite.

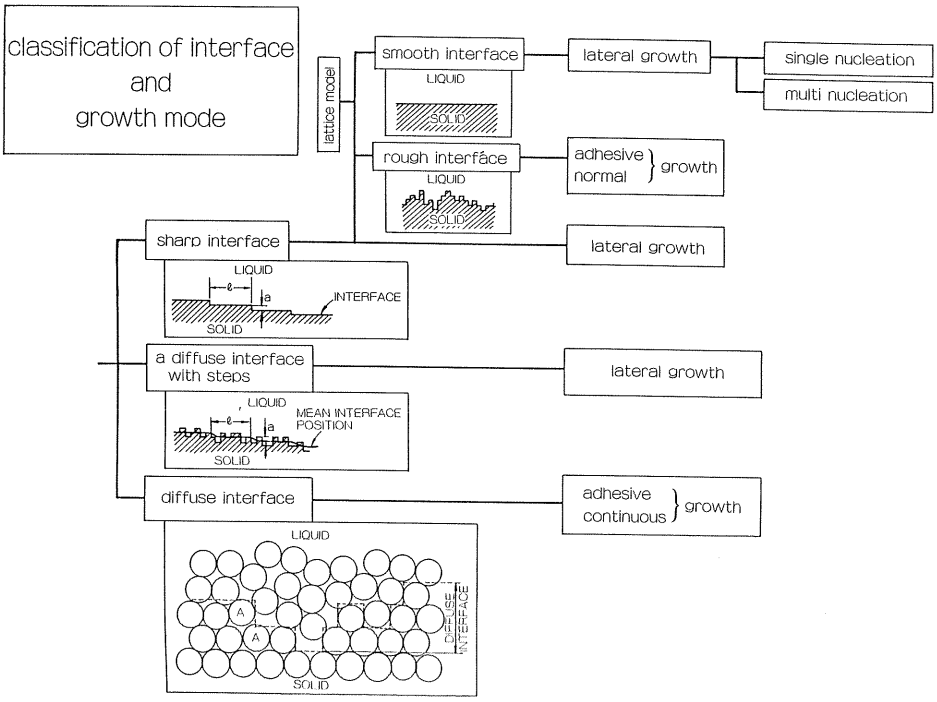

Fig. 40. Schematic illustrations of solid-liquid interface and growth mechanism.

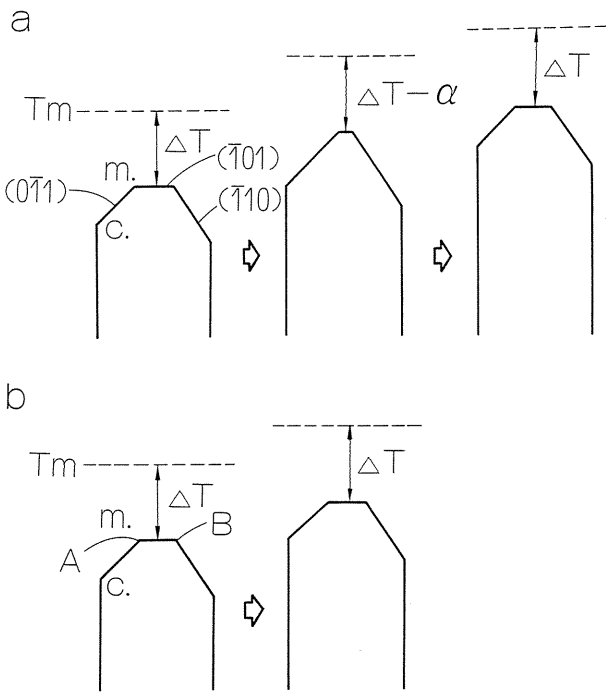

Fig. 41. Schematic illustrations of faceted interface observed in the solidification process. (a) is for the case of growth on a singular interface with a low rate of nucleus spread and (b) for the case of a singular interface with rapid lateral spread. The dotted line indicates the isothermal plane in the melt. ΔT : supercooling.

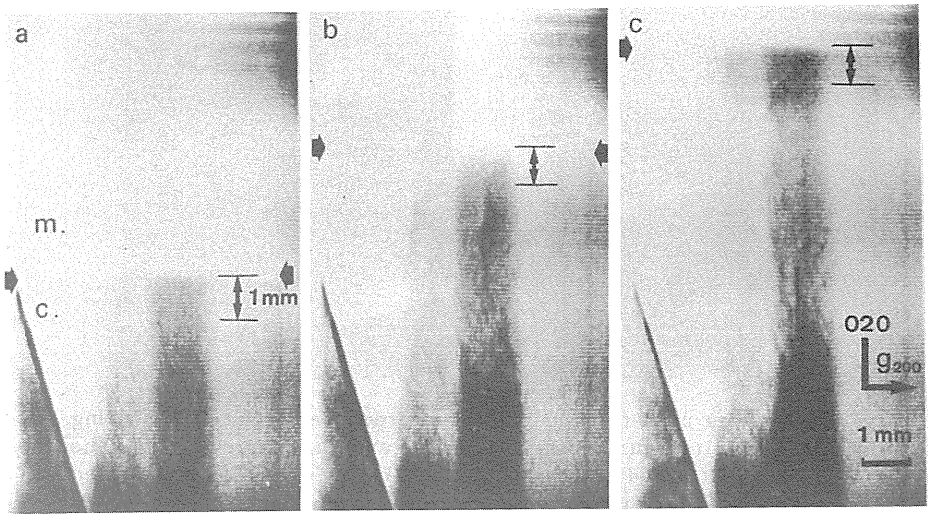

Fig. 42. A series of x-ray topographs showing growth process of an Al single crystal. (99.999% pure).

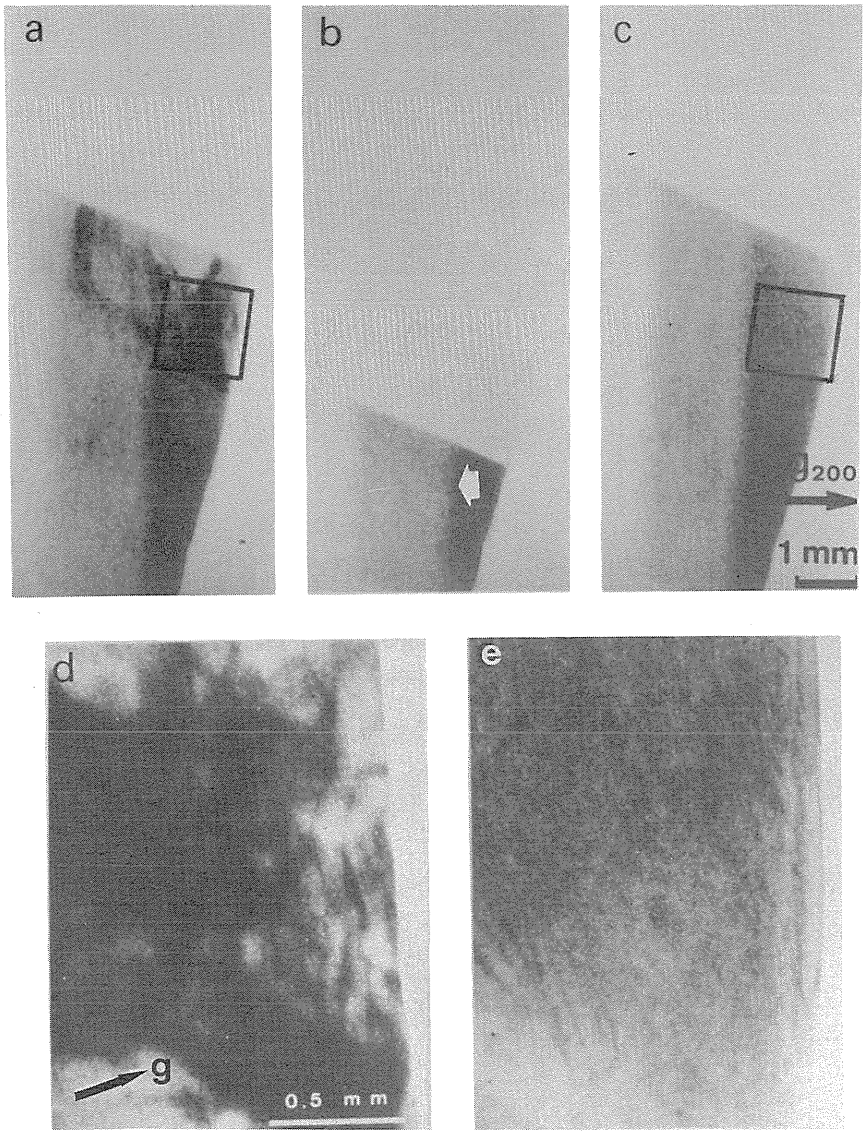

Fig. 43. A series of x-ray topographs recorded on a video tape during melting (a), in the equilibrium (b) and during growth (c). The images (d) and (f) are magnified images of the area indicated in (a) and (c) which were recorded on nuclear research plates just before melting and just after growth, respectively.

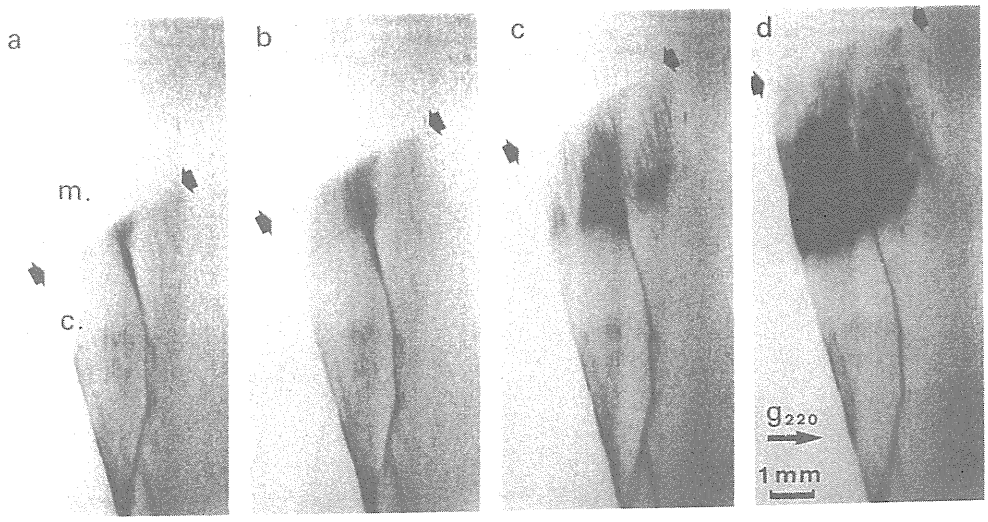

Fig. 44. A series of x-ray topographs (TV images) taken after the change of growth rate from 20 to 42 μm/s in the growth process.

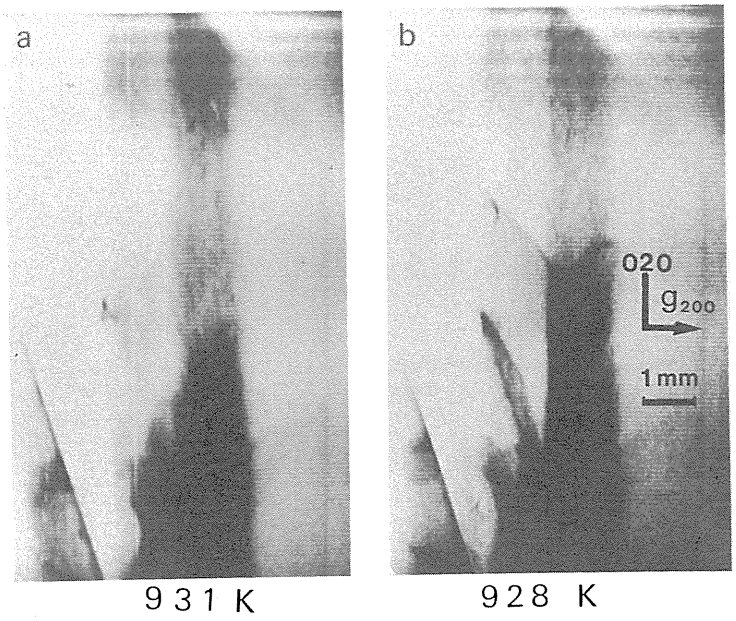

Fig. 45. X-ray topographs of Al (99.999%) taken during cooling process. Temperatures of the top of the crystal are shown below each topograph. Cooling rate was about 5 K/h and the temperature gradient was 1 K/mm.

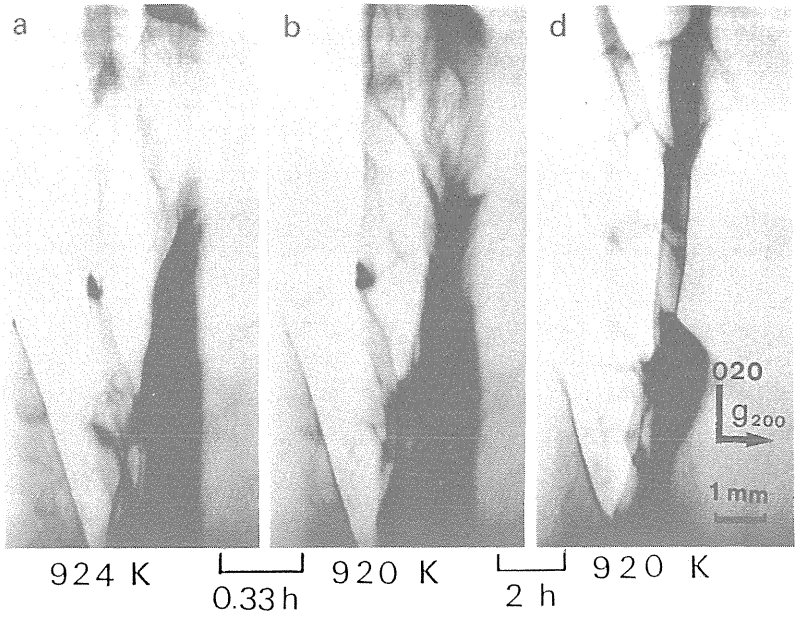

Fig. 46. A series of x-ray topographs taken during sequential cooling to Fig. 45. Temperature of the crystal and the intervals between the successive topographs are indicated below each topograph. The cooling rate between (a) and (b) was 12 K/h.

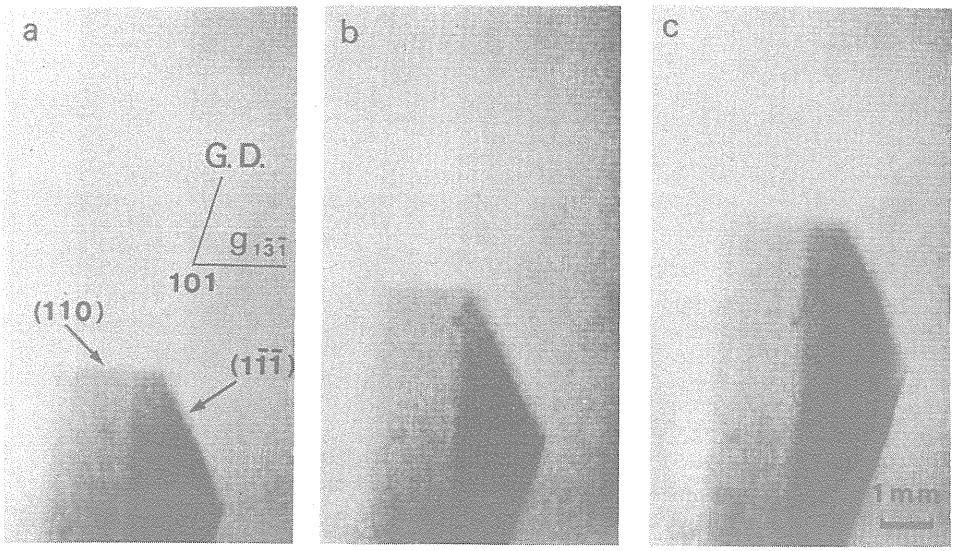

Fig. 47. A series of x-ray topographs (TV images) showing the growth of a gallium single crystal. Growth rate was about 3 μm/s. Facets of (110) and (1$\bar{1}\bar{1}$) planes at the solid-liquid interface are indicated by arrows.

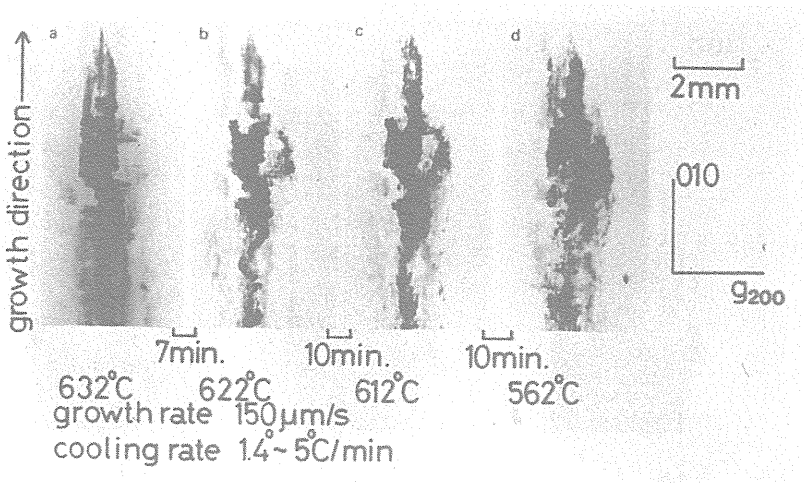

Fig. 48. A series of x-ray topographs of Al-4at.% Mg taken in the cooling process.

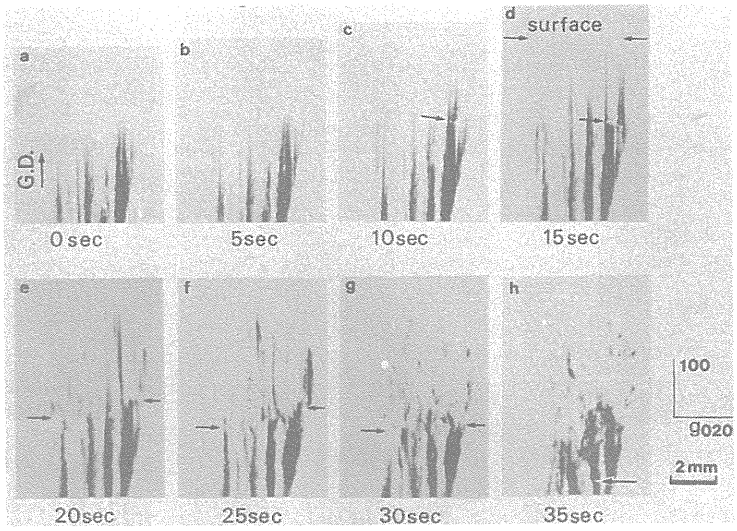

Fig. 49. Morphological change of dendrite arms of Al-4.0 at. % Mg observed during growth ((a)—(d)) and subsequent cooling ((e)—(h)). Cooling rate was about 1 K/s.

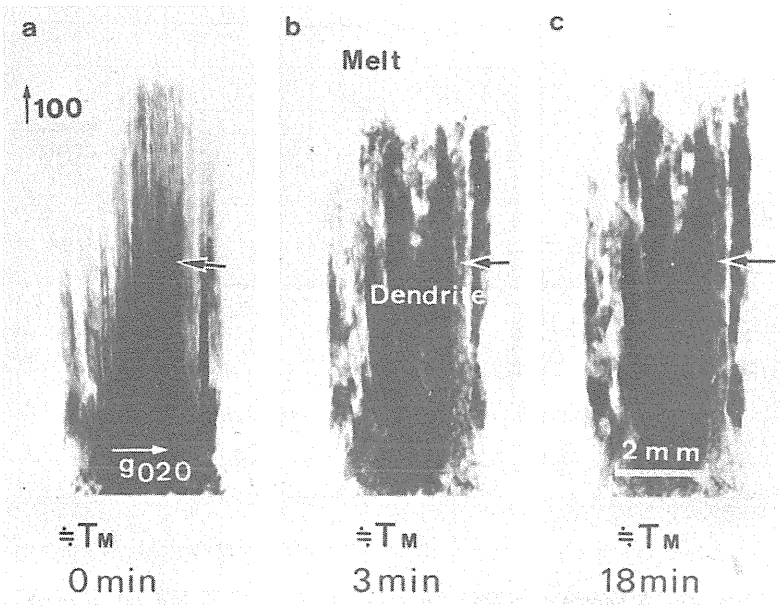

Fig. 50. Morphological change of dendrite arms of Al-4 at. % Mg observed during isothermal annealing near the melting point after solidification. (a) was taken just after solidification, and (b) and (c) were taken after the crystal was kept for 3 and 18 minutes, respectively. The images were recorded on nuclear research plates.

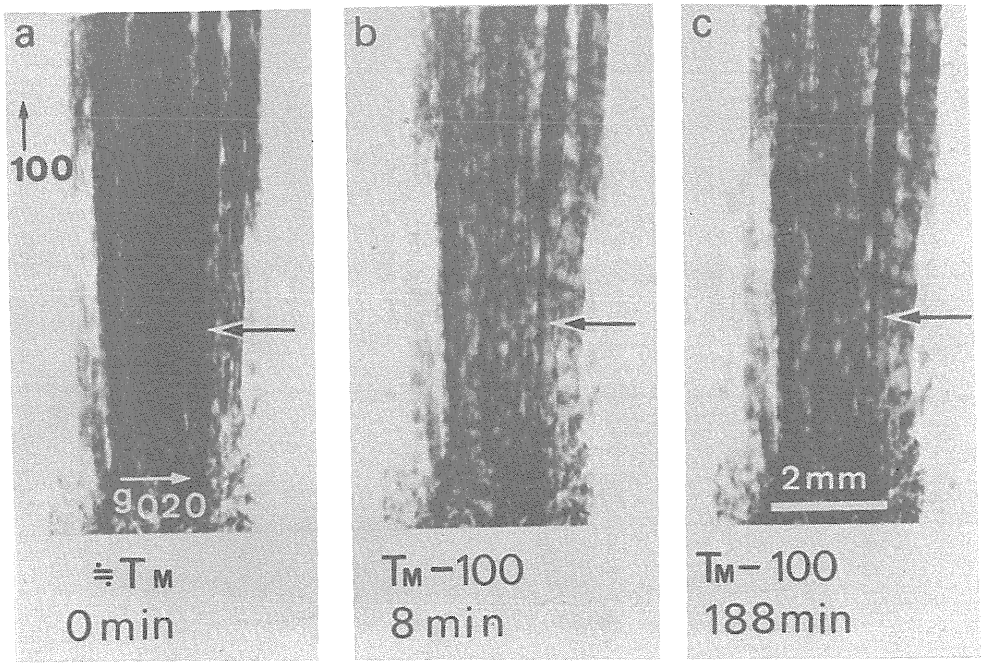

Fig. 51. X-ray topographs of Al-0.5 at.% Mg showing the morphological change of dendrite by isothermal annealing at T_M-100℃.

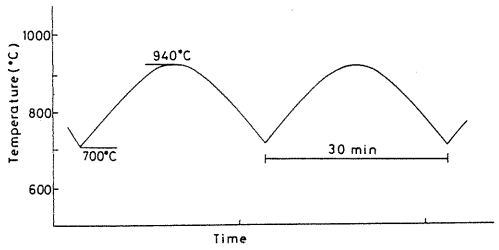

Fig. 52. The temperature change at a point on the specimen surface during the thermal cyclic annealing.

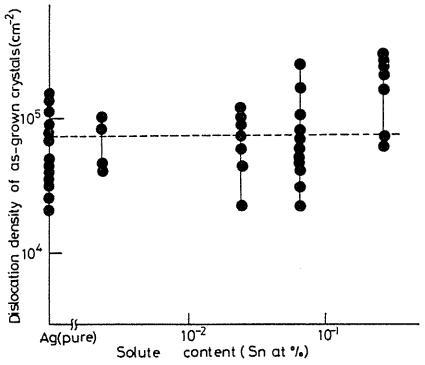

Fig. 53. The effect of Sn content on the dislocation density of as-grown crystals.

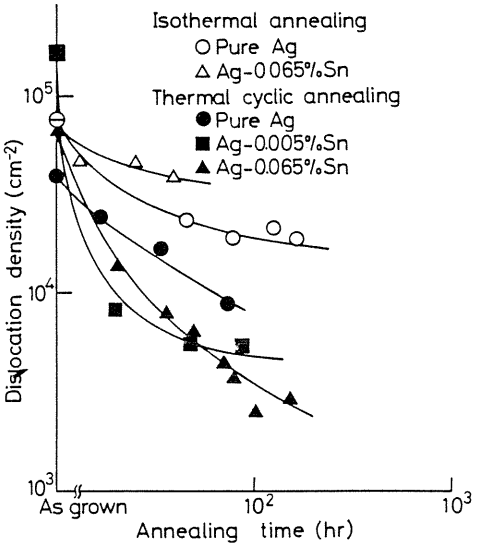

Fig. 54. Effects of the total annealing time on the average dislocation density in pure Ag and Ag-Sn alloys.

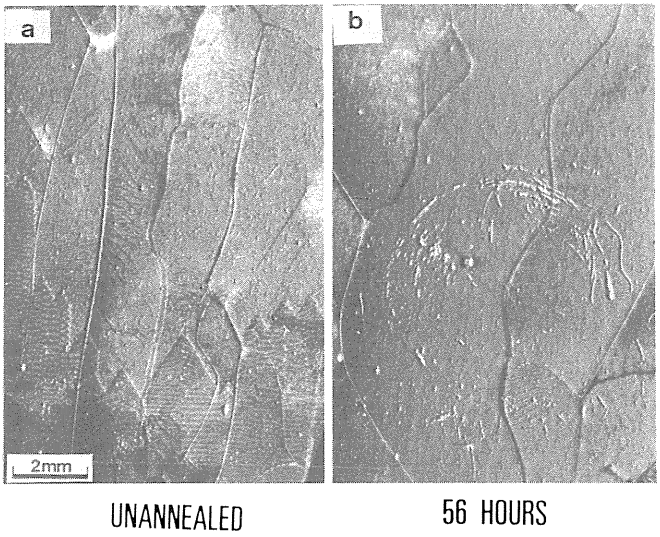

Fig. 55. X-ray topographs of an Fe-Si specimen annealed isothermally at 1350℃ for 56h. a) Before annealing, b) after annealing; density of dislocations in subgrains is reduced remarkably, but the subgrains do not disappear completely.

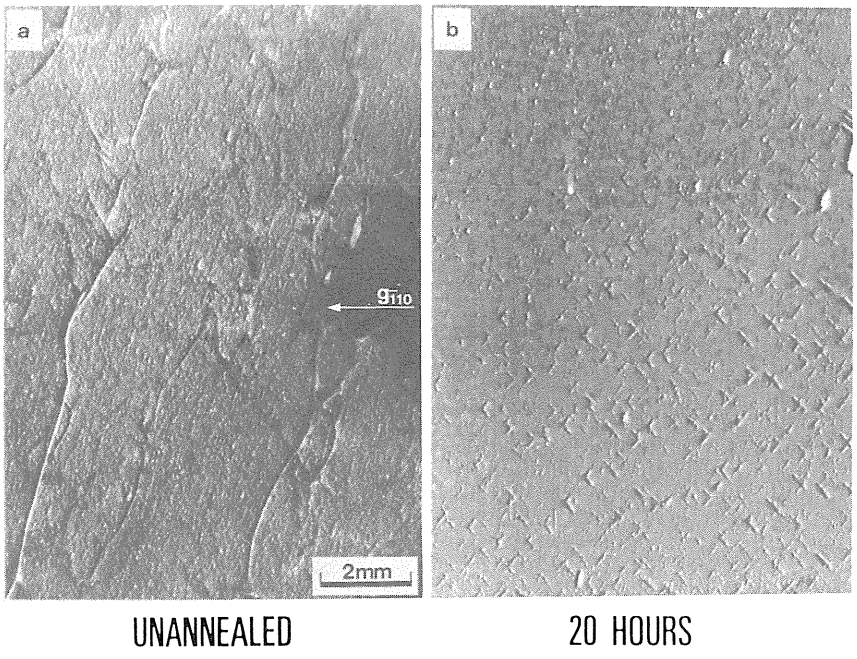

Fig. 56. X-ray topographs of an Fe-Si specimen annealed thermocyclically between 1100 and 1350℃ for 20h. a) Before annealing, b) after annealing; the subgrains have disappeared completely, and the density of dislocations is very low.

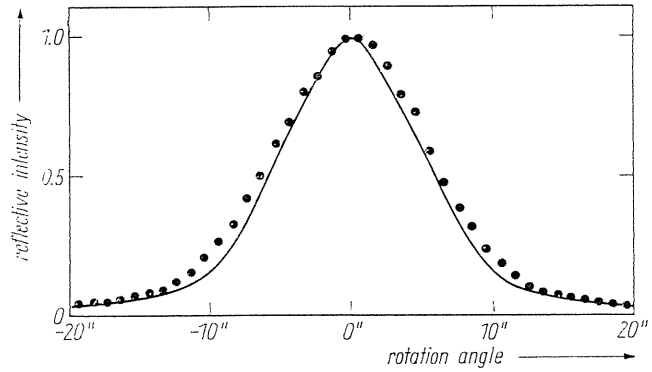

Fig. 57. Rocking curve of 110 reflection obtained by a double-crystal-method. The theoretical curve is also shown by a solid line. The half-width value obtained experimentally is as small as 13".

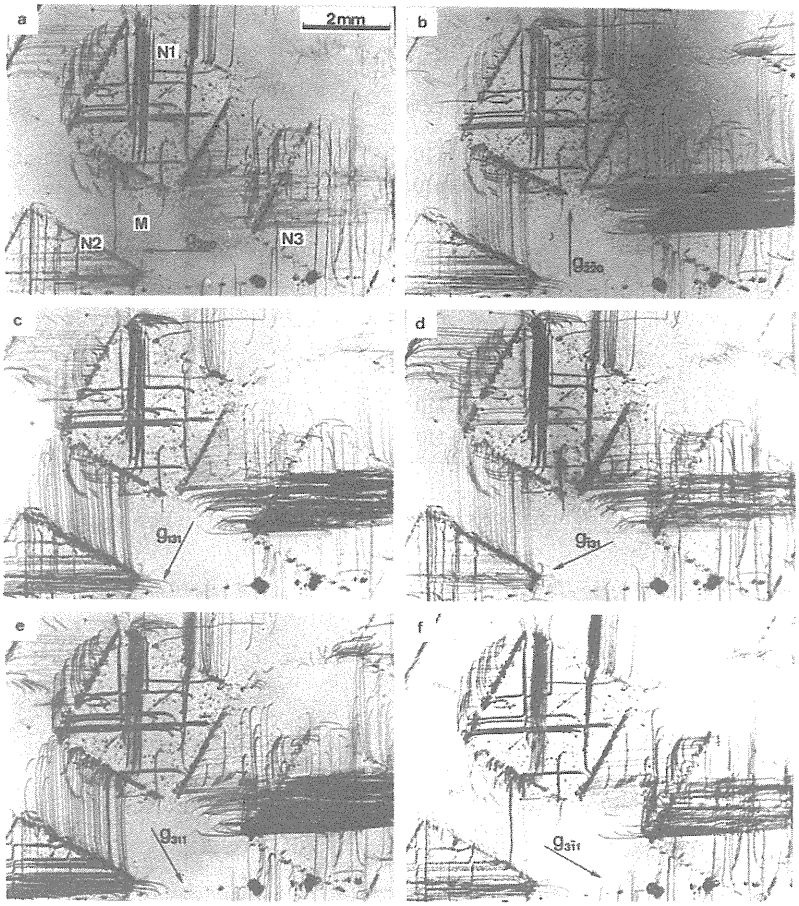

Fig. 58. X-ray topographs of an FZ Si wafer before a thermal cycle annealing taken at the same area under different diffracting vectors g. The Si_3N_4 film was deposited on the areas denoted by N1, N2, and N3, while the remainder denoted by M was masked during the deposition of S_3N_4.

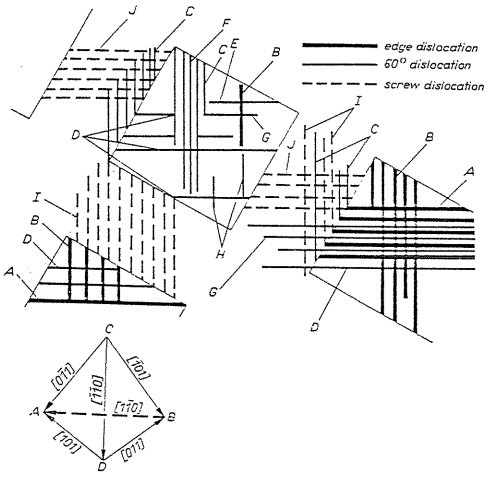

	b parallel to	dislocation-line direction	nature in Thompson's notation	character
A	110	110	DC	edge(Lomer)
B	110	110	BA	edge(Lomer)
C	101	110	DA(β)	60°
D	101	110	DA(β)	60°
E	101	110	BC(δ)	60°
F	011	110	BD(α)	60°
G	011	110	DB(γ)	60°
H	011	110	CA(β)	60°
I	110	110	DC	screw
J	110	110	AB	screw

Fig. 59. Summary of the contrast experiments shown in Fig. 58.

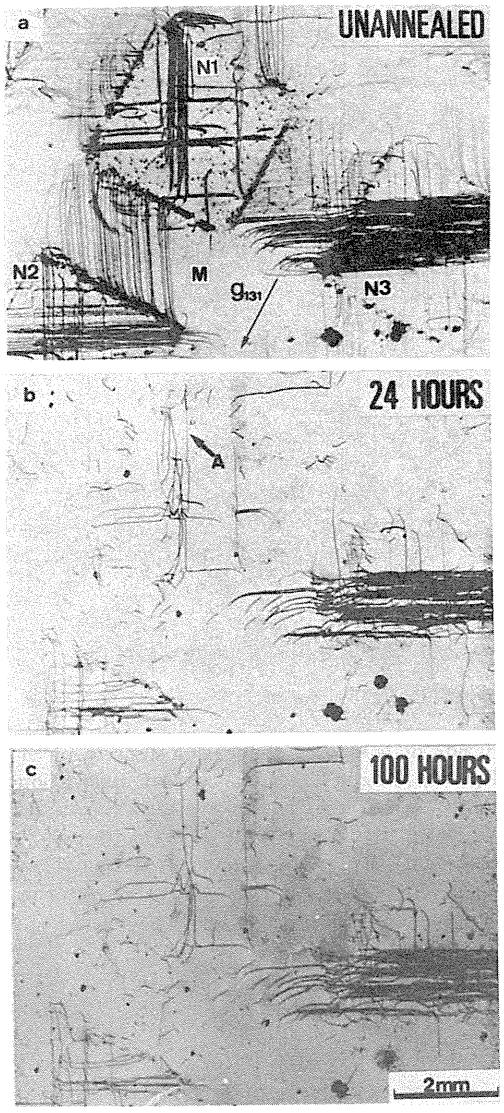

Fig. 60. Variation of dislocation structures of Si during thermal cyclic annealing for b) 24 h and c) 100h. a) unannealed.

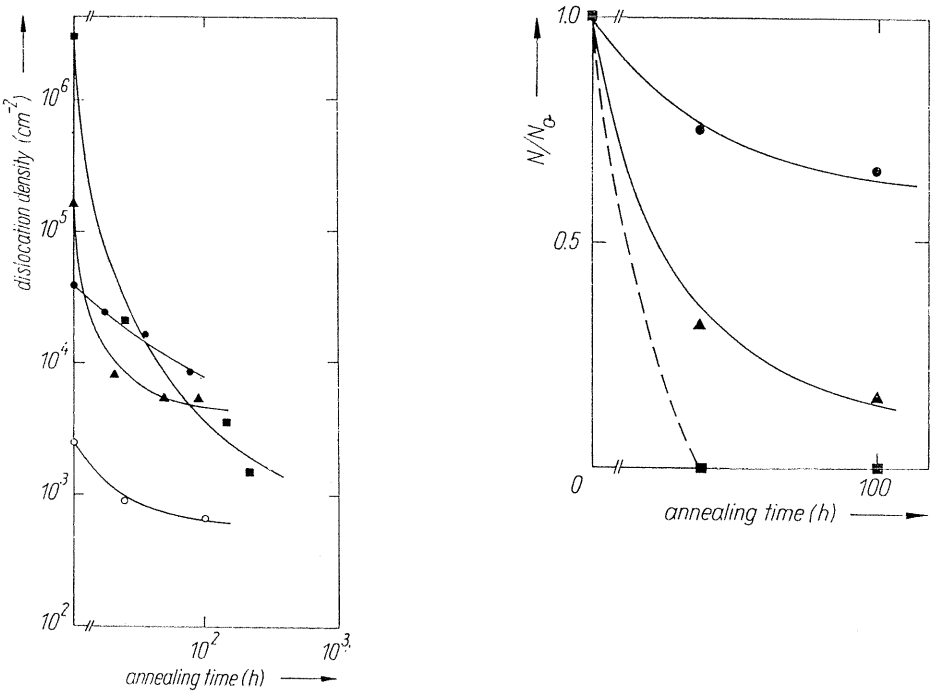

Fig. 61. (a) Variation of the total dislocation density of Si (○) during a thermal cyclic annealing. The variations of dislocation density in Cu(■), Ag (●) and Ag-0.005% Sn (▲) are also shown for comparison.
(b) Variation of the density of Lomer (●), 60° (▲), and pure screw dislocations (■) in Si during a thermal cyclic annealing. The densities (N) are normalized as ratios to the initial densities (N_0) for the respective types of dislocations.